Integrated Nowcasting through Comprehensive Analysis (INCA)

System description

T. HAIDEN, A. KANN, G. PISTOTNIK, K. STADLBACHER,
AND C. WITTMANN

Central Institute for Meteorology and Geodynamics, Vienna, Austria

04 January 2010

CONTENTS

1. Introduction

A common characteristic of numerical weather prediction (NWP) models is that their forecast errors in the nowcasting range (up to +6 hours) are not significantly smaller than those at +12 or +24 hours. This is because NWP model integrations are initialized with analysis fields that are strongly constrained by the model's dynamics and physics and therefore may differ significantly from observed values at observation locations. Moreover, limited horizontal resolution (typically of the order of 10 km) does not allow reproducing all the small-scale phenomena that determine atmospheric conditions at a specific location. In the case of temperature, a simple persistence forecast can be better in terms of mean absolute error (MAE) or root-mean-square error (RMSE) than the NWP forecast for up to several hours (Figure 1.1). One may also construct a temperature forecast based on the climatologically mean diurnal evolution by simply adding it to the latest observed temperature (red curve in Figure 1.1). This simple method can give significantly smaller errors than the NWP model for forecast times of up to +6 h. Because of this 'nowcasting weakness' of NWP models, which is an issue even with today's high-resolution models such as AROME or WRF, it is necessary to complement and improve the NWP forecast by an observation-based analysis and forecasting system such as INCA. The INCA system adds value to the classical NWP forecast by providing (a) high-resolution analyses, (b) nowcasts, and (c) improved forecasts both within and beyond the nowcasting range.

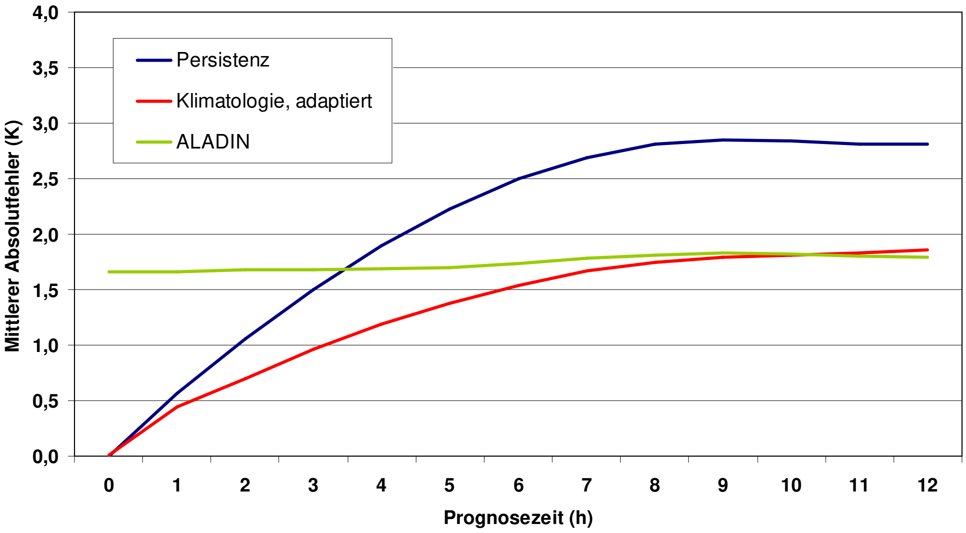

Figure 1.1: Mean absolute error of the 2 m temperature forecast during February 2003 at the station Vienna-Hohe Warte as a function of lead time. Persistence (blue) and persistence+climatology (red) forecasts are significantly better than the NWP model during the first hours.

Many existing observation-based forecasting systems have been developed for the prediction of precipitation and convective activity (Browning and Collier 1989, Li et al. 1995, Hand 1996, Golding 1998, Pierce et al. 2000, Seed 2003). During the World Weather Research Program (WWRP) Forecast Demonstration Project of the 2000 Sydney Olympics several of these methods were tested and compared (Pierce et al. 2004). In the same project, one wind analysis and nowcasting system was tested and evaluated (Crook and Sun 2004). However, research has generally focused not so much on forecasting the wind field as such but its effect on the initiation and development of deep convection (Wilson and Schreiber 1986, Wilson et al. 2004). Similarly, analysis and nowcasting of near-surface temperature (Sun and Crook 2001) and humidity has traditionally been regarded as a means for predicting convective developments and not so much as a value in itself.

On the other hand there is an increasing demand in public and private sectors for high-quality very-short-range forecasts of temperature, wind, global radiation (cloudiness), and precipitation. Real-time flood-warning systems are implemented on the basis of hydrological models that require meteorological input at small scales and short lead times. Transportation planning is increasingly based on meteorological forecasting. Weather services face the challenge of issuing for the general public improved weather warnings at a high update frequency and with more precise geographical specification.

In order to satisfy all these requirements, an analysis and nowcasting system cannot be restricted to stations but needs to be spatially quasi-continuous, i.e. it must operate on a high-resolution grid. It should take into account, as far as possible, all available data sources (model results, station data, radar and satellite data, radiosoundings, etc) and use them to construct physically consistent analyses of atmospheric fields. In a way, it should do something similar to what a human forecaster does when (s)he tries to synthesize all available information, both from NWP and observations, into a consistent forecast. But whereas forecasters can come up with numerical values for only a limited number of locations or regions, an algorithmic system can perform the synthesis on an entire grid. Even so, the algorithmic system will always have the disadvantage of being less complex, and using less data, than the ‘expert system’ represented by the human forecaster who can, for example, look up additional model results on the internet that are not available numerically at the weather service. Thus, INCA is aiding the forecaster in the synthesis of the daily flood of information but certainly neither able nor intended to replace the forecaster. In the case of weather warnings in particular the general policy of ZAMG is to issue warnings only after they have undergone the forecaster’s decision and controlling process.

The following description of the INCA system gives an overview of its general characteristics, geometry, and data sources (Sections 2-4). The analysis and nowcasting components are described in Sections 5 and 6. Source code names as found in the INCA export version are given in brackets (blue) in the Section titles **[program.c]**. Subroutine names are given as well [subroutine()], with the description of the relevant equations. Settings of logical switches are given in green [LOGSWITCH=1]. It should be emphasized that INCA is a relatively young system still under development. While individual components and concepts used in INCA have been developed earlier (Haiden 1997, 1998, 2001a) actual work on the operational system has started in spring 2004. Rather than wait for several years until a sophsticated system has been built, the philosophy was to start with a working baseline version to which further improvements and refinements are added in a step-by-step process. This approach has the advantage that (a) forecasters and applications using the baseline version can provide valuable feedback early on, and (b) the baseline version can be used as a benchmark against which the significance of further improvements can be measured.

2. General characteristics

The INCA analysis and nowcasting system is being developed primarily as a means of providing improved numerical forecast products in the nowcasting range (up to +4 h) and very short range (up to about +12 h) even though it adds value to NWP forecasts up to +48 h through the effects of downscaling and bias correction. It should be stressed that the analyses generated by the system are not used as initial conditions for NWP model integrations. Thus the analysis method is not constrained by specific NWP model dynamics or physics. Highly structured fields can be produced both in space and time without causing noise-related adverse effects in a subsequent forecast. Nevertheless, the basic approach to analysis and nowcasting used in INCA is strongly rooted in physical considerations. The computation of the three-dimensional temperature error field for example takes into account a surface-layer contribution to the temperature profile which depends on insolation. This is described in Section 5a.

The methods used for spatial interpolation are simple (distance-weighting in geometrical and physical space). The idea behind this choice is, apart from its straightforward implementation, that the system should be as transparent as possible and the number of ‘climatological’ assumptions kept at a minimum. It also makes further developments and improvements easier and allows easier interpretation by the forecaster. The meteorological fields analyzed with INCA are

- Temperature (3-d)
- Humidity (3-d)
- Wind (3-d)
- Precipitation (2-d)
- Precipitation type (2-d)
- Cloudiness (2-d)
- Global radiation (2-d)

There is limited inter-dependency between fields. For example, in the nowcasting of temperature the cloudiness analysis and nowcast is taken into account. The surface cooling effect of thunderstorm cells due to evaporation of precipitation is considered in the analysis and nowcasting of temperature. However, more of these physically evident interactions will be considered in the further development of INCA (thus the ‘I’ for ‘integrated’). The temperature, humidity, and wind analysis will be used to assess the initiation and evolution of convective cells (Steinheimer and Haiden 2007).

In addition to the quantities listed above, derived fields are computed. These fields are mostly convective parameters such as lifted condensation level (LCL), convective available potential energy (CAPE), or equivalent potential temperature. Other derived fields are snowfall line and surface temperature needed for precipitation type (snow, rain, snow/rain mix, freezing rain), as well as icing potential, which is still in the experimental stage. Using snowfall line, forecasts of snowfall accumulation (water equivalent) are generated.

The high resolution of 1 km is a crucial characteristic of INCA. It enables the system to take most station observations at ‘face value’, since at this resolution the actual elevation and exposition of a station coincide to a large degree with their counterparts on the numerical grid. A wind observation at a mountain pass, for example, will not be representative of conditions a few km away because of acceleration of the flow through the pass. If this observation is used to create a high-resolution 3-d wind field analysis it is important that the analysis system is able to simulate the characteristics of the location. Only then can a kinematic or dynamic downscaling procedure make proper use of the local wind observation.

From topographic maps it can be seen that a resolution of 1 km is required to resolve major alpine valleys in a way that the modelled valley floor is close to the actual valley floor height. It is a sufficient resolution to approximately reproduce slope inclinations on the sidewalls of major valleys. Side-valleys, however, are represented in a smoothed way, even at 1 km resolution. It will be part of further studies with INCA to determine the potential benefit of having even higher resolution. Another reason for using the 1 km grid is that it corresponds to the resolution of the radar data used in INCA. If we would use a coarser grid, some of the details provided by the radar data regarding the fine structure of convective cells would be lost.

One of the main conceptual differences between INCA and another Austrian analysis system VERA (Steinacker et al., 2006) is that INCA analyses use NWP model information for interpolation between observations, whereas VERA uses climatological information through a fingerprint method.

3. Coordinate system [setup_inca_topo.c, inca_proj.f]

In the horizontal, a Lambert conical projection (Bessel ellipsoid) is used, with reference latitudes 46° and 49° N, and a central reference point at 47°30’ N, 13°20’ E. The central reference point has the Cartesion coordinates *x*=400 km, *y*=400 km on the projection grid. The coordinate system has been adopted from the Austrian Bundesamt für Eich- und Vermessungswesen (BEV). It is also used by hydrological research groups at Austrian universities with which ZAMG cooperates in the development on flood warning systems (Komma et al. 2007). The current domain of the INCA system consists of an area of 600×350 km at a resolution of 1 km (601×351 gridpoints). It covers the eastern Alps and alpine forelands (Figure 3.1).

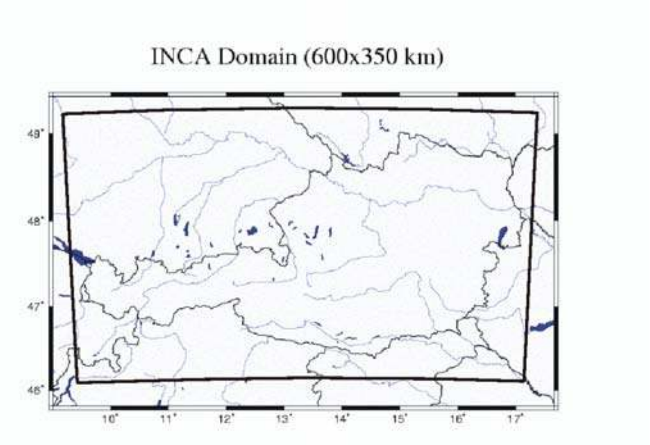

Figure 3.1: INCA analysis and nowcasting domain. Resolution is 1 km.

In the vertical, a *z*-system is used where *z* is the height above the ‘valley floor surface’ shown schematically in Figure 3.2. In mountainous or hilly terrain, the valley floors of adjacent valleys are generally found at comparable heights. Thus one may define a hypothetical surface that is smooth compared to the actual topography and connects major valley floors (Haiden 1998). In other words, the topography is conceptually separated into a base topography and a relative topography. This separation is, of course, not unique, and depends on what is considered a major valley. In practical applications, the valley floor surface is computed objectively by identifying for every gridpoint the minimum elevation within a given radius, and arithmetically smoothing the resulting field over a circle of the same radius. For alpine topography, a radius of 10 km was found appropriate. The resulting valley floor surface (Figure 4.4) represents a useful local reference height. Over completely flat terrain, topography and valley floor surface coincide. The vertical resolution of INCA is currently equidistant at Δz = 200 m. The system has 21 levels (including the surface), thus it covers the lowest 4000 m above the local valley floor surface. For the wind analysis, the

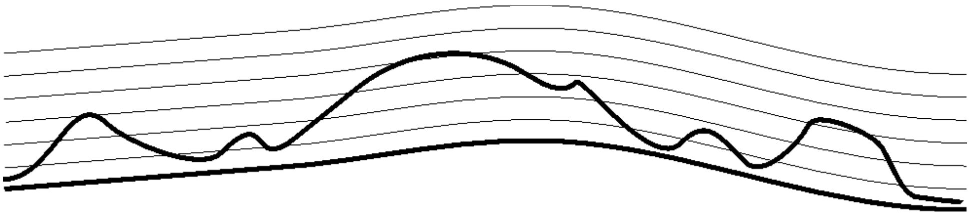

Figure 3.2: Schematic depiction of INCA coordinate surfaces. The vertical coordinate is the height above the valley floor surface, which forms the base of the topography. Vertical resolution is 200 m.

valley floor surface is set to zero, i.e. a true *z*-coordinate with horizontal levels is used. The vertical increment in the case of wind has been set to $\Delta z = 125$ m.

4. Data sources

4.1 NWP model output

For the three-dimensional INCA analyses of temperature, humidity, and wind, NWP forecast fields provide the first guess on which corrections based on observations are superimposed. For this purpose the output of the limited area model ALADIN is used which has been run operationally at ZAMG since 1999. The NWP fields are 1-hourly, at a resolution of 9.6 km, with 45 levels in the vertical (Wang et al. 2006). However, the INCA analysis and nowcasting methods do not depend critically on the horizontal resolution of the NWP fields and could as well be based on other NWP models. The Swiss version INCA-CH, for example, uses COSMO fields as a first guess.

At ZAMG, four ALADIN forecast runs per day are performed (00Z, 06Z, 12Z, 18Z). The 00Z and 12Z runs are integrated to +72 h, the 06Z and 18Z runs to +60 h. Post-processed fields are available roughly 4 h after analysis time. ALADIN forecast fields used in INCA are geopotential, temperature, relative humidity, u-, v-, w- wind components (3-d fields), 2m temperature and relative humidity, u-, v- 10m-wind components, precipitation, total cloudiness, low cloudiness, and surface temperature (2-d fields). The three-dimensional fields are provided on pressure surfaces with a vertical resolution of 50 hPa up to 600 hPa, and a resolution of 100 hPa above. The domain of the ALADIN model is shown in Figure 4.1.

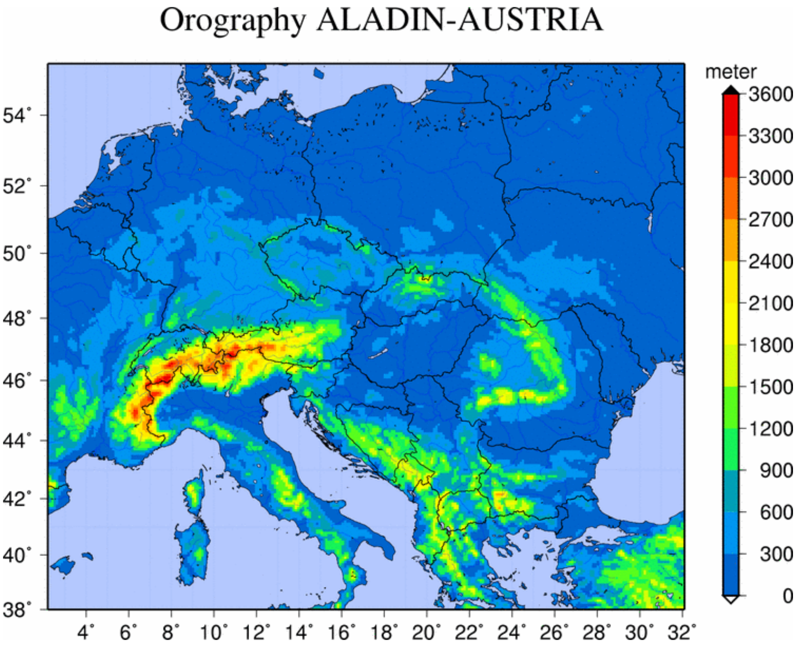

Figure 4.1: Model domain and topography of ALADIN-AUSTRIA. Horizontal resolution is 9.6 km.

4.2 Surface station observations

The single most important data source for the INCA system are surface stations. ZAMG operates a network of ~200 automated stations (Teilautomatisches Wetterstationsnetz, TAWES) across the country. In the vertical, this network spans most of the topographic range in Austria, with highest stations Brunnenkogel (3440 m), and Sonnblick (3105 m).

Although the distribution of stations is biased towards valley locations there is a sufficient number of mountain stations to construct three-dimensional correction fields to the NWP model output, based on observations. The station density versus elevation roughly corresponds to the area-height distribution of the topography up to about 1500 m. At higher elevations, the station density is lower than it ideally should be according to the area-height distribution.

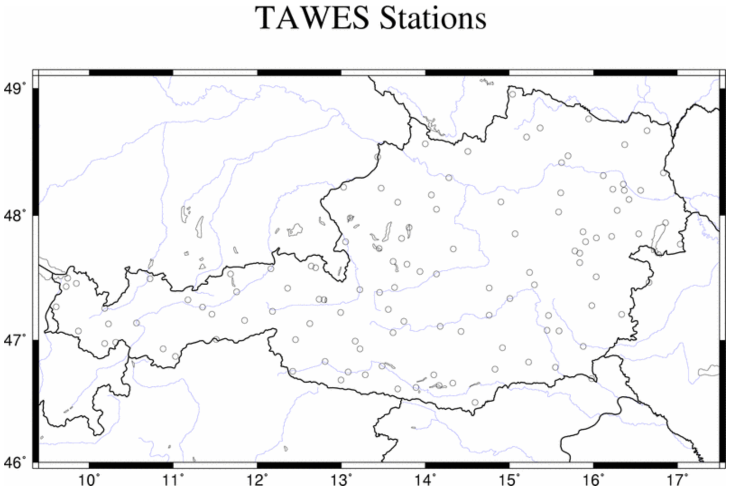

Figure 4.2: Location of TAWES surface stations.

TAWES stations take measurements in 1 min intervals. The data is sent to ZAMG in Vienna in 10-min intervals. For the INCA precipitation analysis, which works on a 15 min update frequency, the 1 min precipitation amounts are accumulated. The meteorological observations used in INCA are 2m temperature, relative humidity and dewpoint (measured independently), 10m wind, precipitation amount, precipitation minutes, and insolation minutes.

There are other surface meteorological stations which are increasingly used by the INCA system. The hydrological service of Austria operates a network of hydrometeorological stations, of which ~150 could provide precipitation and temperature data for real-time analyses on a 15-min basis. At the time of this writing, the hydrometeorological stations of the provinces of Lower Austria, Salzburg, Tyrol, and Carinthia have already been integrated into the operational precipitation analysis system. This gives a roughly two-fold increase in station density in those areas (Figure 4.3a). For the hourly temperature and humidity analysis, SYNOP stations from neighbouring countries, as well as hydrological stations from Tyrol, Salzburg, Carinthia, and Lower Austria are available (Figure 4.3b).

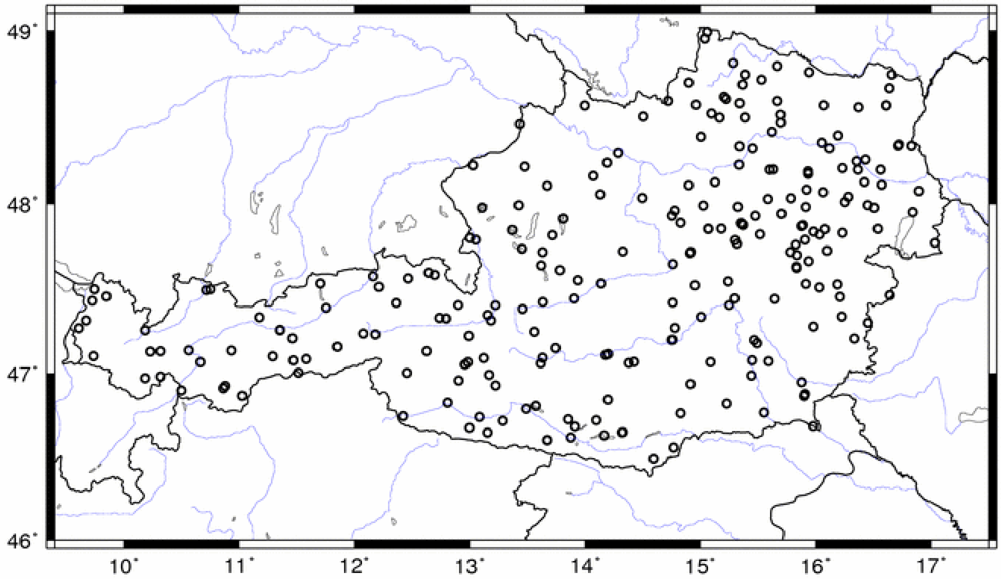

Figure 4.3a: Stations used operationally in the 15-min INCA precipitation analysis (TAWES stations + hydrological stations).

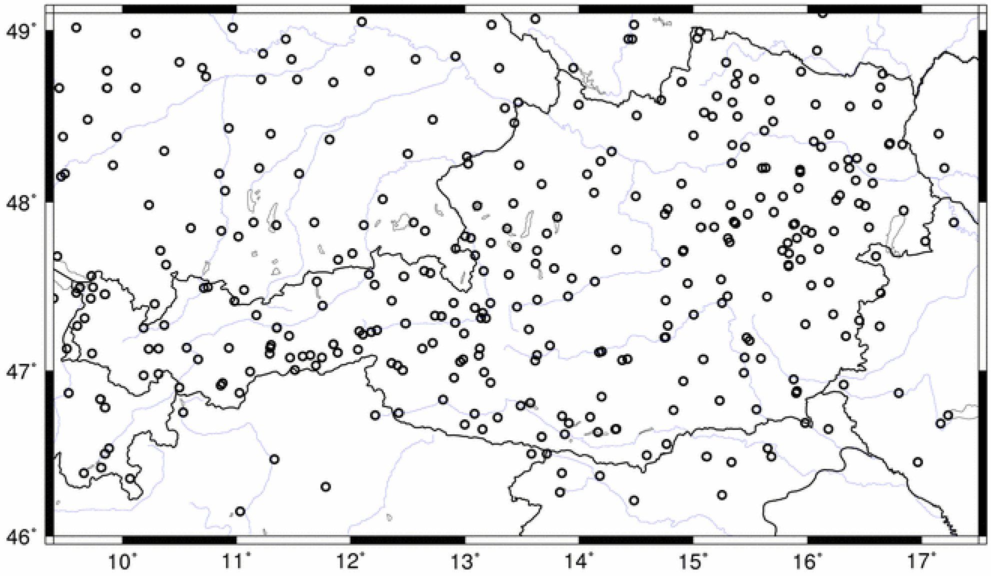

Figure 4.4b: Stations used operationally in the 1-h INCA temperature and humidity analysis (TAWES stations + SYNOP stations + hydrological stations).

4.3 Radar data

The Austrian radar network is operated by the civil aviation administration (Austrocontrol). It consists of four radar stations located at the Vienna airport, near the city of Salzburg, near the city of Innsbruck (on Patscherkofel mountain), and in northeastern Carinthia (on Zirbitzkogel mountain). ZAMG operationally obtains 2-d radar data synthesized from these 4 locations, containing column maximum values in 14 intensity categories, at a time resolution of 5 minutes. Ground clutter has already been removed from the data. However, due to the mountainous character of the country, radar data is of limited use in many areas in western Austria, especially during wintertime, when precipitation may originate from rather shallow cloud systems.

4.4 Satellite data

The Meteosat 2nd Generation (MSG) satellite products used in INCA are ‘Cloud Type’ which consists of 17 categories, and the VIS image. Cloud type differentiates between three cloud levels (low, medium, high) as well as different degrees of opaqueness. It also diagnoses whether clouds are more likely convective or stratiform in character. The VIS image is used to downscale the infrared-based (and thus coarser resolution) cloud types during the day.

4.5 Elevation data

The 1-km topography used in INCA (Figure 4.3) was obtained through bilinear interpolation from the global 30’’ elevation dataset provided by the US Geological Survey. The resolution of 30’’ of the original dataset corresponds to ~930 m in latitudinal, and ~630 m (at 48°N) in longitudinal direction.

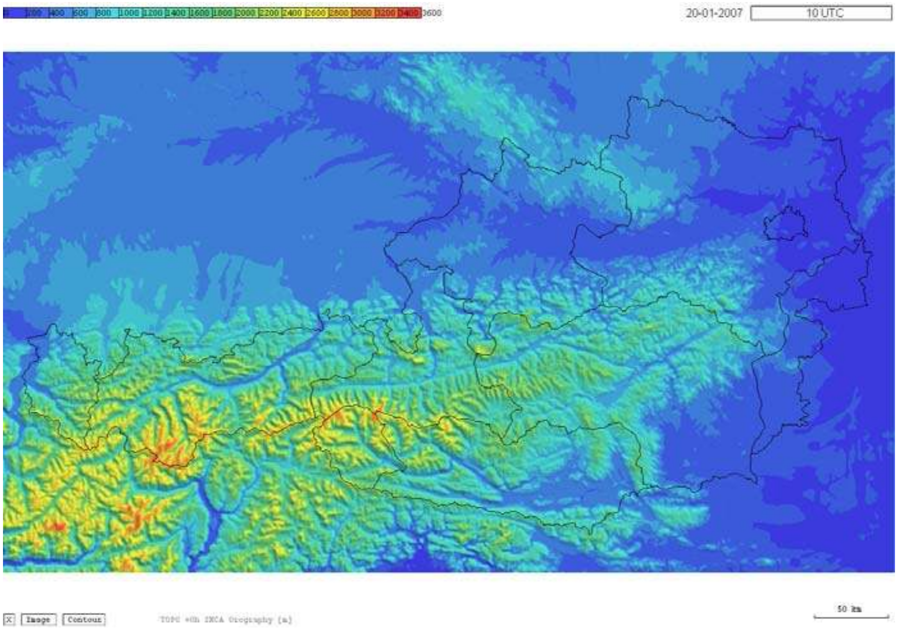

Figure 4.3: INCA topography.

4.6 Derived topographic fields [setup_inca_topo.c]

For the extrapolation of 3-d ALADIN forecast fields into valleys, a ‘valley floor surface’ (Figure 4.4) is derived from the elevation dataset. It represents the mesoscale average height of valley floors and is computed by assigning to every gridpoint the minimum elevation found within a radius of 10 km. The resulting field is smoothed with a running average 20km×20km window.

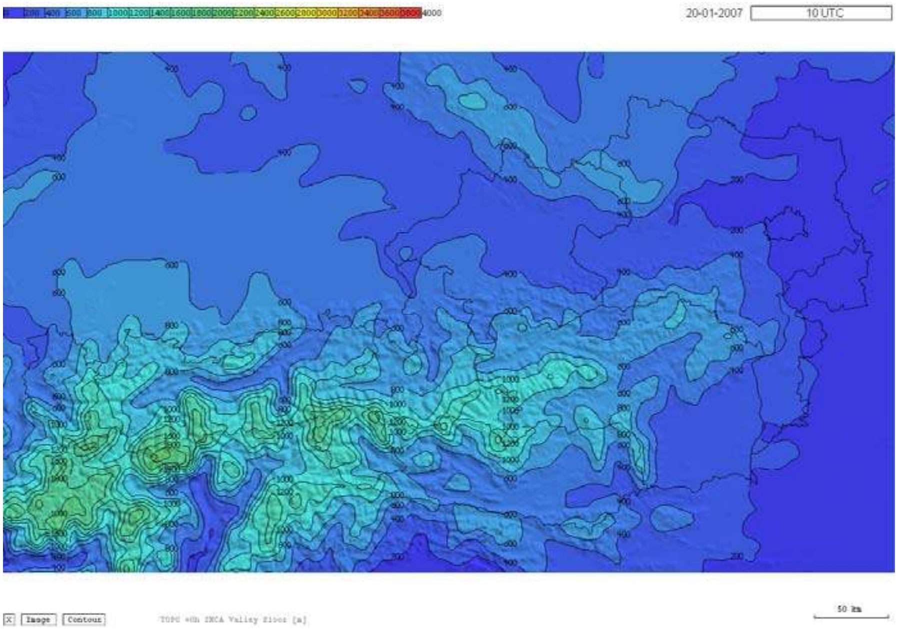

Figure 4.4: INCA valley floor surface.

Another derived topographic field is a nondimensional surface layer index I_{SFC} which varies between 0 and 1. It is used in the temperature and humidity analysis and characterizes the extent to which the local terrain supports the formation of a distinct surface layer. It is computed as follows. First, for every gridpoint the average height of the topography within a square window of 7×7 points (6×6 km²) centered around the gridpoint is determined, but only for those points within the window that are at a lower elevation than this gridpoint. The difference between the gridpoint elevation $z(i,j)$ and this ‘average height of the surrounding lower topography’ $\overline{z(i,j)}^{l}$ is a measure of how topographically exposed a gridpoint is (Fig. 4.5). If it is exposed (such as high on a slope, or on a peak), the formation of a distinct surface layer with large values of temperature deficit or surplus will be inhibited due to synoptic-, meso-scale, and slope flows. If it is not exposed (such as at the bottom of a basin), the development of a surface layer will be much more pronounced. We will find stronger surface inversions there at night and a larger near-surface temperature surplus during the day. The nondimensional surface layer index is formulated as a linear function of the height difference $z(i,j)-\overline{z(i,j)}^{l}$ in the form

$$I_{SFC}(i,j) = \max\left[0, \min\left(1, 1-\frac{z(i,j)-\overline{z(i,j)}^{l}-z_{SCALE}}{z_{SCALE}}\right)\right], \tag{4.1}$$

where the scaling parameter z_{SCALE} is currently set to a value of 150 m. From (4.1) it follows that I_{SFC} =1 up to 150 m above valley floor, decreasing linearly to I_{SFC} =0 at a height of 300 m above valley floor. Figure 4.6 shows the resulting field of I_{SFC}. It is 1 on flat terrain, valley floors, and in basins, and 0 on elevated mountain slopes, ridges and peaks. Figure 4.7 illustrates the temperature analysis under stable conditions produced by this method.

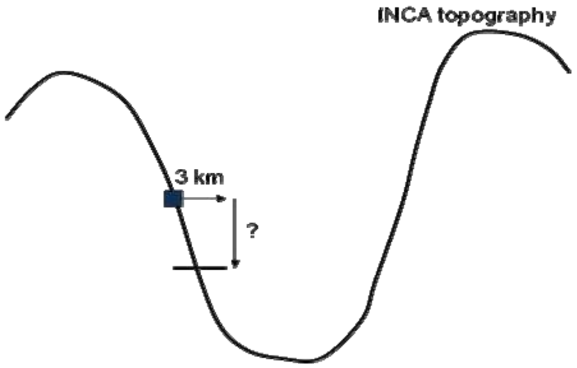

Figure 4.5: The surface layer index I_{SFC} is based on the difference between the local elevation (blue square) and the average elevation of lower lying points (horizontal line).

It is evident that the heuristic method just described can give only a rough approximation to actual temperature profiles in mountain valleys if inversions are present. It could be improved somewhat by replacing the fixed parameter z_{SCALE} by climatological values varying from region to region. Even better, however, would be the use of high-resolution (polar orbiting) satellite observations of surface temperature in the diagnosis of inversion tops. This is one of the planned developments in the INCA temperature analysis. Of course it would only be available if no middle or high level clouds are present.

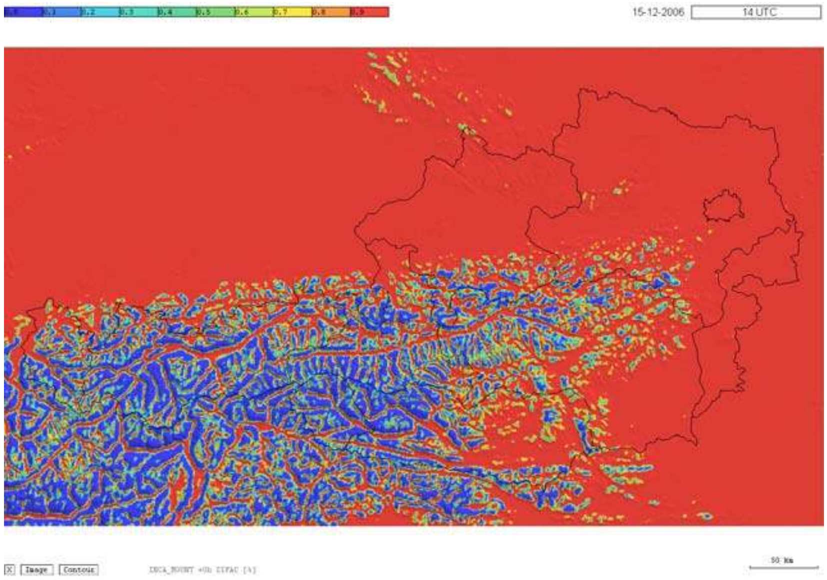

Figure 4.6: INCA surface layer index as computed by (4.1). Red indicates values >0.9 characterizing valley and basin floors, and flat terrain. Dark blue indicates values <0.1 characterizing mountain slopes, ridges and peaks.

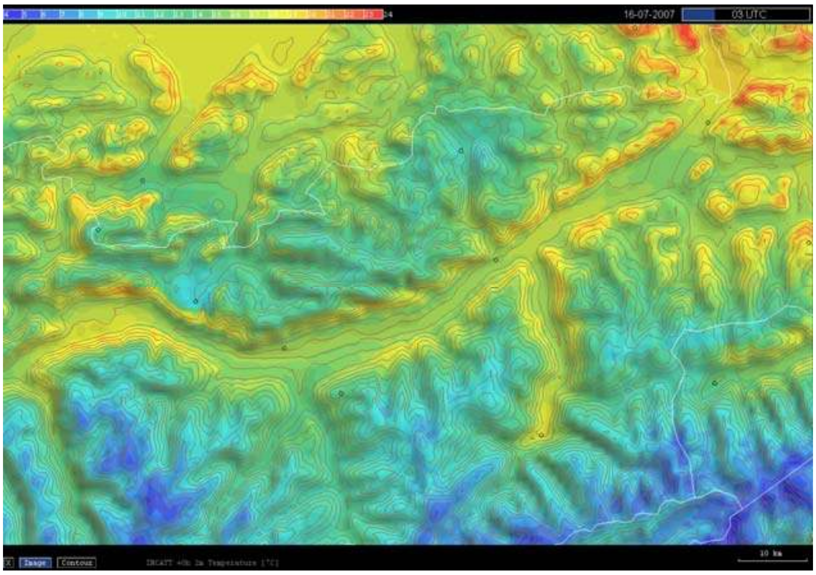

Figure 4.7: Example of an INCA 2m temperature analysis under stable conditions. Use of the surface layer index allows to reproduce warm slope zones with colder air below, and the normal decrease of temperature above.

5. The INCA analysis system

5.1 Temperature and humidity [nwp2inca.c, inca_tq.c]

The three-dimensional analysis of temperature and humidity in the INCA system starts with the ALADIN forecast as a first guess. This first guess is corrected based on differences between observation and forecast at surface station locations. Since the station observations are all made in the atmospheric surface layer it is important to take the daytime temperature surplus and the nighttime temperature deficit near the surface into account in the interpretation of these differences. Thus the ALADIN 2m-temperature forecast is conceptually and computationally separated into a ‘3-d’ or model-level part, and a 2-d surface-layer contribution

$$T^{ALA} = TL^{ALA} + DT^{ALA} . \qquad (5.1.1)$$

Here, T^{ALA} is the standard ALADIN 2m-temperature output, and TL^{ALA} is the temperature at the lowest model level. In practice, we work with 3-d ALADIN output on pressure levels, and TL^{ALA} is obtained by interpolating the 3-d temperature forecast vertically to the height of the model topography. The difference DT^{ALA} between the two temperatures is the temperature surplus (or deficit) in the surface layer. A partitioning analogous to (5.1.1) is done for specific humidity.

To construct the first guess, ALADIN forecasts of temperature and specific humidity on pressure levels are interpolated trilinearly onto the 3-d INCA grid described in Section 3. Special care must be taken in alpine valleys because large parts of the valley atmosphere below ridge level are not represented in the ALADIN model. This is due to its resolution (9.6 km) and aggravated by the fact that an envelope orography is used. The temperature first guess in those parts of the mountain atmosphere is determined by shifting the boundary-layer temperature profile down to the valley floor surface (Figure 5.1.1). The temperature gradient for this downward extrapolation is determined as follows. Within the lowest layer of depth H_{EXT} in the ALADIN forecast, temperature gradients are determined over successively higher height intervals of thickness H_{EXT}/2. The most unstable gradient found

$$\gamma = \min\left(\frac{T\left(z_s^{ALA} + (\frac{i}{n}+1) H_{EXT}/2 \right) - T\left(z_s^{ALA} + \frac{i}{n} H_{EXT}/2 \right)}{H_{EXT}/2} \right) \qquad i = 0,..,n \qquad (5.1.2)$$

is subsequently modified according to

$$\gamma^* = \gamma - f_{EXT} \frac{DT^{ALA}}{H_{EXT}/2} \qquad (5.1.3)$$

in order to account for the increase or decrease in stability indicated by the surface-layer contribution DT^{ALA} [create_vzgrid()]. Here z_s^{ALA} denotes the height of the ALADIN topography, and n=5 the number of intervals over which the gradient is computed. We use the most unstable gradient in order to avoid erroneous extrapolations in cases of strong surface-based or elevated inversions. The parameters H_{EXT} and f_{EXT} were calibrated by verification against observations at those valley stations for which a downward extrapolation of at least 500 m is necessary (~70 stations). Calibration results, including both nighttime and daytime situations, suggest values around H_{EXT}=1000 m, and $f_{EXT}\approx$0.1. For specific humidity, a similar downward profile shift is performed. The gradient obtained from a procedure analogous to (5.1.2)-(5.1.3) is additionally reduced by a factor of f_{QRED} before it is used in the downward extrapolation. Calibration results suggest that a value around f_{QRED}=0.5 gives the smallest errors.

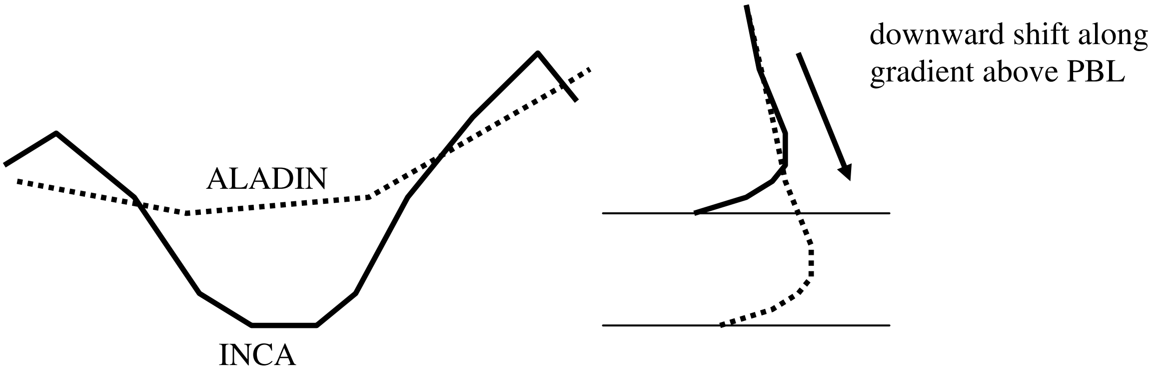

Figure 5.1.1: In valley atmospheres not represented in the ALADIN forecast, the PBL temperature profile is shifted down to the valley floor surface, along the gradient above the PBL.

Next, corrections to the first guess are computed based on differences between observed temperature and the ALADIN temperature forecast at station locations. Like the forecast in (5.1.1) these corrections are conceptually and computationally partitioned into a 3-d model-level part and a 2-d surface-layer contribution

$$\Delta T = \Delta TL + \Delta DT \ . \qquad (5.1.4)$$

While the partitioning in (5.1.1) was implicitly contained in the ALADIN forecast, the partitioning (5.1.4) of corrections must be estimated. The question can be stated as follows: If there is a difference between temperature observation and forecast at a surface station (Fig. 5.1.2), to what extent does it reflect a forecast error that extends to higher levels, and to what extent is it just a forecast error within the surface layer? Here we use the principle of 'minimal required correction'. We assume that a forecast error is restricted to the surface layer as long as this assumption is physically plausible. Only if the forecast error is too large to be explained solely in terms of surface layer differences, then part of it is classified as 3-d model-level error.

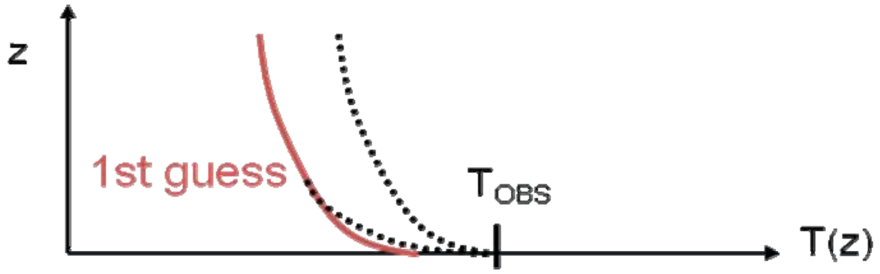

Figure 5.1.2: A difference between observed temperature and the first guess may be restricted to the surface layer (left dotted curve) but it may also extend higher up (right dotted curve).

Following this principle, the 3-d part of the temperature correction at the *k*-th station is computed from

$$\Delta TL_k = \max\left[0, T_k^{OBS} - \max\left(TL_k^{ALA} + DT_k^{ALA}, TL_k^{ALA} + DT_{SCALE}\right)\right] \qquad (5.1.5a)$$

if $T_k^{OBS} \geq TL_k^{ALA}$, and from

$$\Delta TL_k = \min\left[0, T_k^{OBS} - \min\left(TL_k^{ALA} + DT_k^{ALA}, TL_k^{ALA} - DT_{SCALE}\right)\right] \qquad (5.1.5b)$$

if $T_k^{OBS} < TL_k^{ALA}$. The parameter DT_{SCALE} is a near-surface temperature surplus (or deficit) scale which is by default set to 1 K but may have larger values depending on insolation and wind speed (Appendix A). It represents the minimum amount of correction that is assigned to the surface layer, in cases where such a correction is required.

The following example illustrates how the partitioning of the error using (5.1.5a) works. Let us assume that a temperature of $T_k^{OBS} = 15$ °C is observed at a station, and that the observed insolation and wind speed at the station are such that the near-surface temperature surplus is $DT_{SCALE} = 2$ K. Let us further assume the ALADIN model-level forecast is $TL_k^{ALA} = 13.5$ °C and the 2m-temperature forecast is $T_k^{ALA} = 16$ °C, which means the model predicts a surface layer temperature surplus of $DT_k^{ALA} = 2.5$ K. Inserting the values into (5.1.5a) gives

$$\Delta TL_k = \max\left[0, 15.0 - \max\left(13.5 + 2.5, 13.5 + 2.0\right)\right] = 0 .$$

Thus we would conclude in this case that there is no correction required to the 3-d level temperature of ALADIN, and that there is just 1.5 K overheating in the surface layer which, if added to the model level temperature of 13.5 °C, gives the observed 15 °C. If the observed temperature would be $T_k^{OBS} = 17$ °C instead of 15 °C, then (5.1.5b) would give a 3-d level temperature correction of ALADIN of +1 K. Added to the model level temperature of 13.5 °C, this would give a corrected model level temperature of 14.5 °C, which together with the surface temperature surplus of 2.5 K gives the observed 17°C. To summarize, we attribute errors as long as it is physically plausible to the surface layer (2-d), and only if this cannot account for the whole error, we attribute the remaining part to the model-level (3-d) temperature.

Since the beginning of 2007, the surface layer index I_{SFC} as described in Section 4.6 and illustrated in Figure 4.5 is used, and the correction equations (5.1.3a,b) are used in the form

$$\Delta TL_k = \max\left[0, T_k^{OBS} - \max\left(TL_k^{ALA} + I_{SFC,k} DT_k^{ALA}, TL_k^{ALA} + I_{SFC,k} DT_{SCALE}\right)\right] \quad (5.1.5c)$$

if $T_k^{OBS} \geq TL_k^{ALA}$, and

$$\Delta TL_k = \min\left[0, T_k^{OBS} - \min\left(TL_k^{ALA} + I_{SFC,k} DT_k^{ALA}, TL_k^{ALA} - I_{SFC,k} DT_{SCALE}\right)\right] \quad (5.1.5d)$$

if $T_k^{OBS} < TL_k^{ALA}$ [create_t3d_diffs()]. It reduces the amount of correction attributed to the surface layer at slope, ridge, and peak locations.

The 3-d corrections ΔTL_k obtained from (5.1.5c,d) are then spatially interpolated (Fig. 5.1.3). In the horizontal, geometrical distance weighting is used, while in the vertical the distance weighting is performed in potential temperature space. The three-dimensional squared 'distance' between INCA gridpoint (i,j,m) and the k-th station is given by

$$r_{ijmk}^2 = (x_k - x_i)^2 + (y_k - y_j)^2 + c^2(\theta_k^{ALA} - \theta_{ijm}^{ALA})^2 \quad (5.1.6)$$

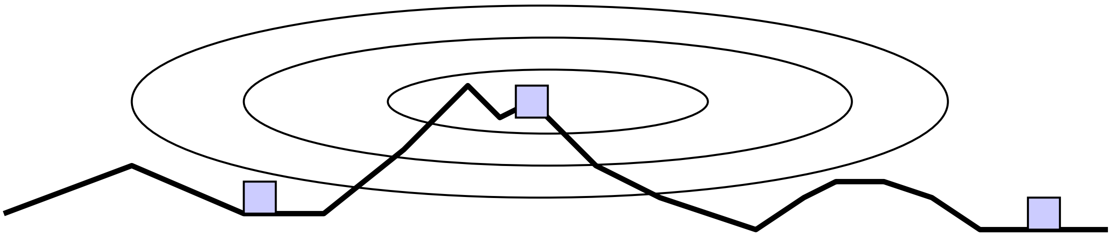

Figure 5.1.3: Schematic depiction of the strength of influence of a station observation. The ratio of the horizontal to vertical distance of influence is determined by station distance and static stability (Eq.(5.1.6)).

where the parameter *c* has the dimension of an inverse temperature gradient. Based on cross-validation its optimum value for both temperature and humidity was found to be close to 3·10^4 m/K. This means that a distance of 1 K in potential temperature space is equivalent to a horizontal distance of 30 km.

The interpolated three-dimensional temperature difference field at gridpoint *i,j,m* is obtained from

$$\Delta TL(i,j,m) = \frac{\sum_{k=1}^{n} \frac{\Delta TL_k}{r_{ijmk}^2}}{\sum_{k=1}^{n} \frac{1}{r_{ijmk}^2}} \quad (5.1.7)$$

[interpolate_t3d_diffs()], where the number of nearest stations used in the interpolation is $n = 8$. Note that 'nearest' in this context means smallest distance in the sense of (5.1.6). Cross-validation has shown this number to give the smallest analysis errors. The temperature difference field is then added to the ALADIN 3-d level temperature forecast, giving

$$TL^{INCA}(i,j,m) = TL^{ALA}(i,j,m) + \Delta TL(i,j,m)\,. \tag{5.1.8}$$

The potential temperature weighting has the important effect that model errors as indicated by station observations are not unphysically interpolated or extrapolated across stable layers.

As a next step, the remaining differences, i.e. those attributed to the surface layer, are determined from

$$\Delta DT_k = T_k^{OBS} - TL_k^{INCA}, \tag{5.1.9}$$

[create_t2m_diffs()] and interpolated horizontally, using a modified inverse distance weighting which takes into account the difference between inversion factors at grid point (*i,j*) and at the location of the *k*-th station

$$\Delta DT(i,j) = \frac{\sum_k \frac{f_{ijk}}{r_{ijk}^2}\Delta DT_k}{\sum_k \frac{f_{ijk}}{r_{ijk}^2}}\;, \tag{5.1.10}$$

where

$$r_{ijk}^2 = (x_k - x_i)^2 + (y_k - y_j)^2\,, \tag{5.1.11}$$

$$f_{ijk} = 1 - \left| I_{SFC}(i,j) - I_{SFC,k} \right| \tag{5.1.12}$$

[interpolate_t2m_diffs()]. The use of (5.1.12) ensures that corrections derived at a certain type of location (e.g. valley floor) are not interpolated to different types of location (e.g. slope). The final 2m temperature analysis is obtained by adding the surface-layer correction (5.1.10) to the corrected model-level field (5.1.8) at the topography height *z*

$$T^{INCA}(i,j) = TL^{INCA}(i,j,m(z)) + \Delta DT(i,j) \tag{5.1.13}$$

[vzgrid_fields_ana()]. The whole procedure reproduces observed values at the station locations to within 0.1-0.3 K. In cases where stations are only a few km apart and observe significantly different temperatures, the difference will be larger but still <1 K.

A procedure analogous to the one described for temperature is performed for specific humidity. Examples of INCA 2m temperature and humidity fields are shown in Figures 5.1.4 and 5.1.5. Cross-validation results averaged over stable and unstable conditions indicate that the analysis MAE is typically 1-1.5 K in lowland and hilly areas, as well as at exposed mountain locations, and 1.5-2 K in mountain valleys. Under well-mixed conditions the MAE drops below 1 K, both in lowland and mountain areas, reaching values near 0.5 K in areas of good station coverage. Largest errors occur in deep mountain valleys under stable conditions. Insufficient knowledge of the height of cold air pools and associated inversions leads to large uncertainty in the temperature, depending on whether a station is still within the cold air or already in warm air, e.g. due to Foehn effects.

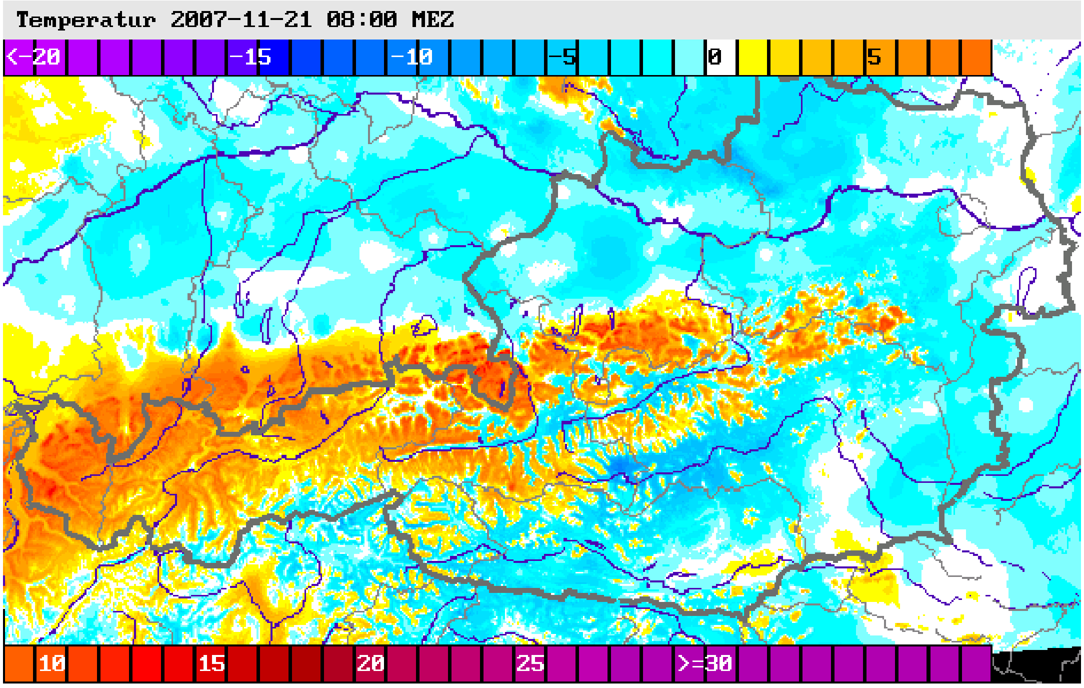

Figure 5.1.4: Example of an INCA temperature analysis during a Foehn situation (21.11.2007, 08Z). Note the asymmetry between northern and southern alpine valleys. Also, the eastern valleys on the north side still have cold air pools in them while the Inn and Rhine valleys are already warmer. Highest temperatures are found on the slopes above the cold air pools.

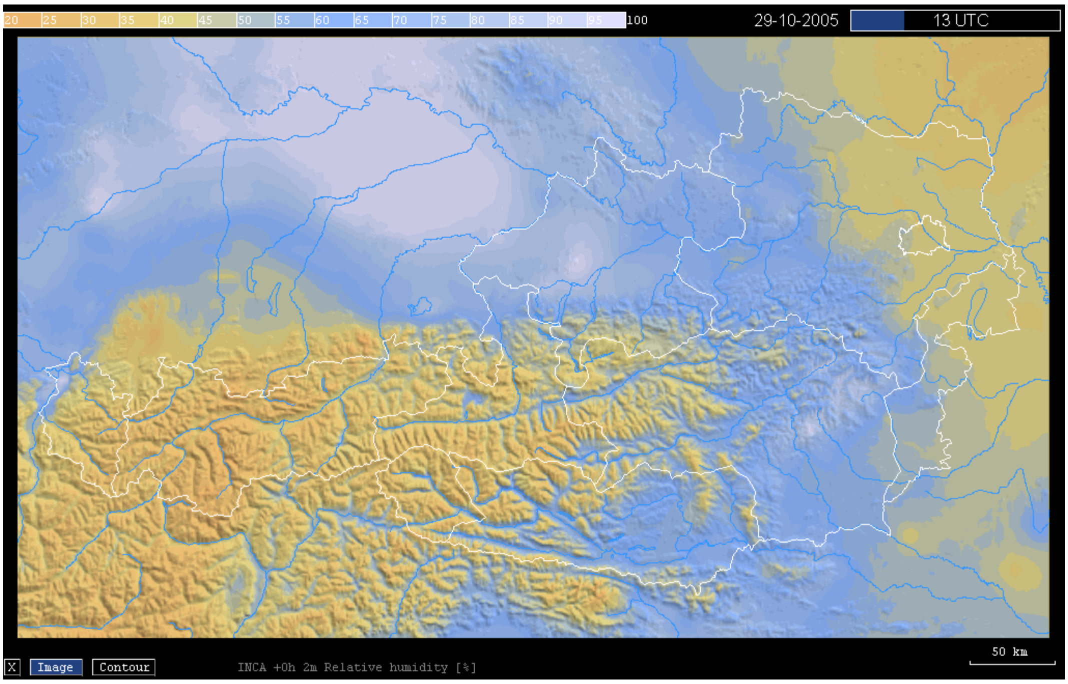

Figure 5.1.5: Example of an INCA humidity analysis (29.10.2005, 13Z). Shown is 2m relative humidity. Typical for autumn, there is a large contrast between cool, humid air in valleys and very dry air above. Note the difference between the Rhine valley in the extreme west, where relative humidity is still high, and the Inn valley, which is already much drier.

The INCA analysis system is designed to take into account the effect of lakes on 2m temperature [LAKEMODE=1]. This is described in Appendix B.

Another effect on temperature which is considered [PRECMODE=1] is the evaporative cooling due to precipitation, which becomes most significant in the case of isolated convective cells on hot days. The amount of cooling is computed as a function of precipitation rate and boundary-layer humidity as described in Section 5.4 [inca_rr.c]. It is given to the temperature analysis as a two-dimensional field $\Delta DT_{PREC}(i,j)$. In the temperature analysis, this cooling is subtracted from the first guess. In the stepwise process (5.1.5)-(5.1.13) this has to be taken into account in several ways. First, TL_k^{ALA} in (5.1.5c,d) is replaced by

$$(TL_k^{ALA})_{PREC} = TL_k^{ALA} - f_{RED,k}\Delta DT_{PREC,k} \qquad (5.1.14)$$

where $\Delta DT_{PREC,k}$ is the value of $\Delta DT_{PREC}(i,j)$ at the location of the *k*-th station, and $0 \le f_{RED,k} \le 1$ is a reduction factor for that location. It becomes relevant in cases where the first guess with cooling effect is further from the observation than the original first guess. If $\Delta DT_{PREC,k} \le$ 1 K, then $f_{RED,k} = 1$ regardless of whether the cooling effect brings the first guess closer to observations. If, however, $\Delta DT_{PREC,k}$ > 1 K, then

$$f_{RED} = \min\left(1, \frac{\left|TL_k^{ALA} - T_k^{OBS}\right|}{\left|(TL_k^{ALA})_{PREC} - T_k^{OBS}\right|}\right). \qquad (5.1.15)$$

Thus, the cooling effect gets reduced if it is not supported by observational evidence. The determination of surface layer differences (5.1.9) assumes the form

$$\Delta DT_k = T_k^{OBS} - \left(TL_k^{INCA} - f_{RED}\Delta DT_{PREC,k}\right), \qquad (5.1.16)$$

and the final combination step (5.1.13) is modified to

$$T^{INCA}(i,j) = TL^{INCA}(i,j,m(z)) - f_{RED}(i,j)\Delta DT_{PREC}(i,j) + \Delta DT(i,j)\,, \qquad (5.1.17)$$

where the gridded $f_{RED}(i,j)$ is obtained by interpolating the values at the stations using inverse squared distance weighting

$$f_{RED}(i,j) = \frac{\sum_k \frac{f_{RED,k}}{r_{ijk}^2}}{\sum_k \frac{1}{r_{ijk}^2}} \qquad (5.1.18)$$

[interpolate_fdt2mp()] with r_{ijk}^2 as defined in (5.1.11).

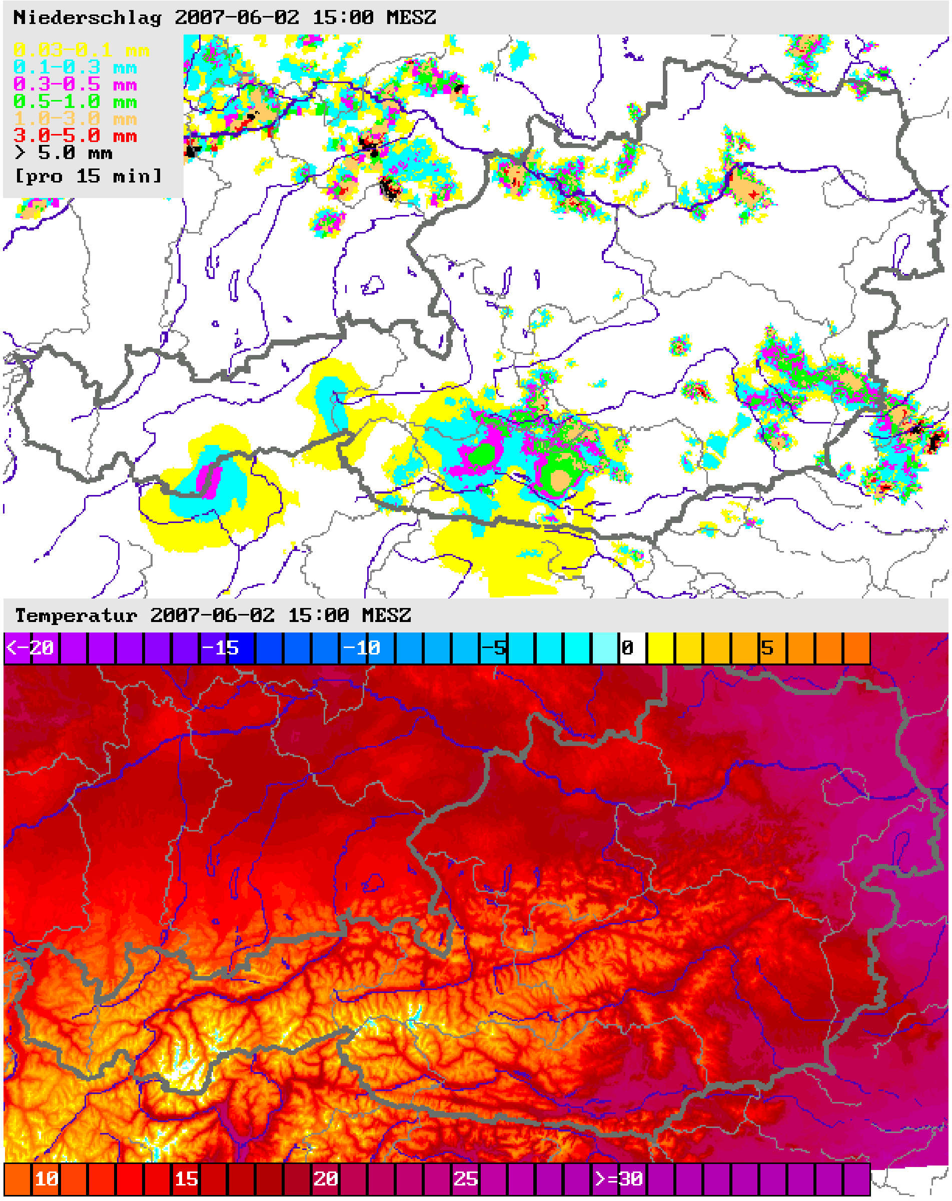

Figure 5.1.5: Example of an INCA 15-min precipitation analysis (top) and its effect on the temperature analysis (bottom). In northern and southeastern Austria the cooling due to convective cells can be seen in the spatial pattern of the temperature analysis.

5.2 Wind [nwp2inca.c, inca_uv.c]

Like the INCA analysis of temperature and humidity, the INCA wind field analysis is three-dimensional, and based on ALADIN fields as a first guess. The ALADIN wind forecast, interpolated to the INCA grid, is used as a background field on which observation increments are superimposed and interpolated. As in the case of temperature and humidity, a distinction is made between the 3-dimensional model-level value of wind speed and the 2-dimensional 10m wind speed of the model. The latter is computed in the NWP model by interpolation, using boundary-layer physics, between the lowest model level and the surface. This 10m wind, however, is the one on the topography of the NWP model, which is not what we want. As in the case of temperature, we interpolate the model-level wind tri-linearly to the topographic height in INCA. The observed wind at a station is of course the 10m wind. So if we determine differences between model-level wind and observations we must estimate the factor f_{10} which translates a model-level wind into a 10m wind. Based on the ratio between 10m wind and model level wind in the ALADIN output it was found that on average $f_{10} \approx 0.75$, which is the value that is used operationally at low levels and in valleys. Higher above the valley floors, where the terrain is more exposed, this factor is assumed to increase to 0.9. The parameterization of f_{10} has the form

$$f_{10}(i,j) = F_{10}^{VAL} + \left(F_{10}^{MTN} - F_{10}^{VAL}\right)\min\left[1, \max\left(0, \frac{z_H(i,j) - z_V(i,j)}{z_{SCALE}}\right)\right], \qquad (5.2.1)$$

where F_{10}^{VAL}=0.75, F_{10}^{MTN}=0.9, z_{SCALE}=300 m, z_H is the topography, and z_V is the valley floor surface.

After multiplying the observed wind by f_{10}^{-1}, differences of the *u*- and *v*-components between model and observations are computed [create_uv3d_diffs()] and interpolated [interpolate_uv3d_diffs()] according to the method illustrated for temperature by Eqs.(5.1.1)-(5.1.3). At this point the resulting 3-dimensional wind field $\vec{v} = (u, v, w)$ is not mass-consistent. First, because the inverse squared distance interpolation of observation corrections does not produce a mass-consistent field, and second, because the ALADIN wind forecast does not fit to the high-resolution INCA topography. An iterative relaxation algorithm [reduce_div()] is applied to obtain a mass-consistent field that satisfies

$$\nabla \cdot (\rho \vec{v}) = 0, \qquad (5.2.2)$$

and the kinematic boundary condition

$$\vec{v} \times \vec{n} = 0 \quad \text{at} \quad z = z_H \qquad (5.2.3)$$

(no flow through the terrain), where $\vec{n}$ is the normal vector of the slope element. In (5.2.2) only the vertical variation of density

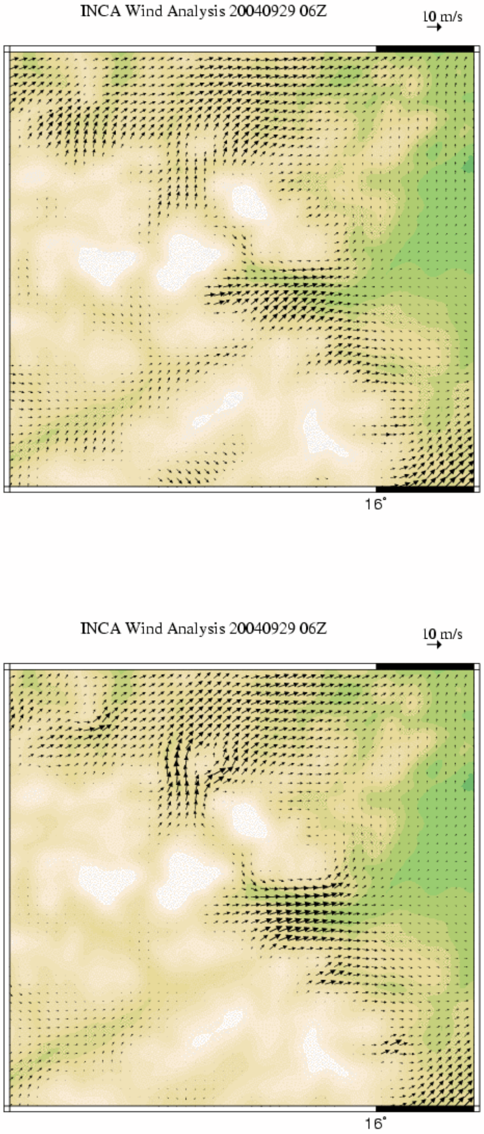

Figure 5.2.1: ALADIN wind forecast at z=1000m in an area at the eastern alpine rim, downscaled to 1 km before (upper panel) and after the relaxation procedure (lower panel). Note the channeling and acceleration of the flow around some of the mountain flanks and through passes, which is required for mass-consistency.

$\rho = \rho(z)$ is considered. During the relaxation procedure, wind vectors at station locations are kept at their observed values. Figure 5.2.1 shows an example of the wind-field before and after the relaxation procedure. It should be noted that the current downscaling procedure in INCA is purely kinematic. It cannot introduce dynamical flow effects such as mountain waves or foehn into the analysis if these phenomena are not already present in the NWP model field or in the observations.

The coordinate system used in the wind module of INCA is a true *z*-system with horizontal coordinate surfaces intersecting the terrain. There are 32 levels at a constant spacing of 125 m. The irregular shape of grid volumes intersecting the terrain ('shaved elements', Figure 5.2.2) is taken into account [insert_topo()] in the computation of divergence, which is part of the relaxation procedure (Steppeler et al., 2002).

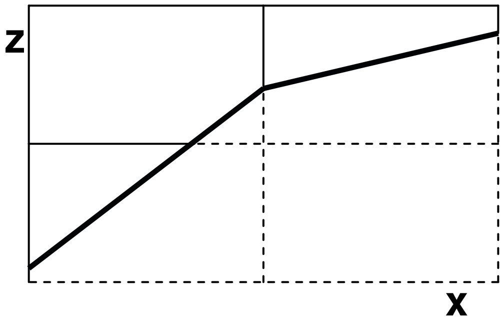

Figure 5.2.2: Coordinate system used in the INCA wind module, showing shaved elements generated by the intersection of *z*-surfaces with terrain (bold line).

The standard output of the INCA wind analysis that is visualized for the forecaster is 10 m wind, as in the example shown in Figure 5.2.3. It is computed from the relaxed wind field, applying the f_{10} factor [vzgrid_fields()]. The example shows highest wind speeds in the lowlands east of the Alps, as well as on mountain ridges and peaks. The zoom shows channelling of the flow in valleys and around mountain flanks.

Over lakes, near-surface wind speeds are generally higher than over the surrounding land, due to reduced roughness length over water as compared to grass, trees, etc. In the INCA system this is taken into account using boundary-layer similarity theory as follows. It was described above that the ratio between ALADIN 10 m wind and model level wind was found to be $f_{10} \approx 0.75$ at low elevations. Using the logarithmic wind profile, and a reference roughness length $(z_0)_{ref}$ =0.1 m, typical of grassland, or farmland, with interspersed trees (Stull, 1988), this value of f_{10} implies an effective model level height of

$$z_{lev} = (z_0)_{ref} \exp\left(\frac{\ln\left(\frac{z_{10}}{(z_0)_{ref}} \right)}{f_{10}} \right) \approx 46\,\text{m}, \tag{5.2.4}$$

where z_{10} = 10 m. Using the 10 m wind u_{10} generated by INCA without lake effects, friction velocity u_* is computed from the logarithmic wind profile

$$u_* = \frac{k\, u_{10}}{\ln\left(\frac{z_{10}}{(z_0)_{ref}} \right)}, \tag{5.2.5}$$

where *k* = 0.4 is von Karman's constant. The modified value of f_{10} over the lake is then given by

$$(f_{10})_{lake} = \frac{\ln z_{10} - \ln z_0}{\ln z_{lev} - \ln z_0}, \tag{5.2.6}$$

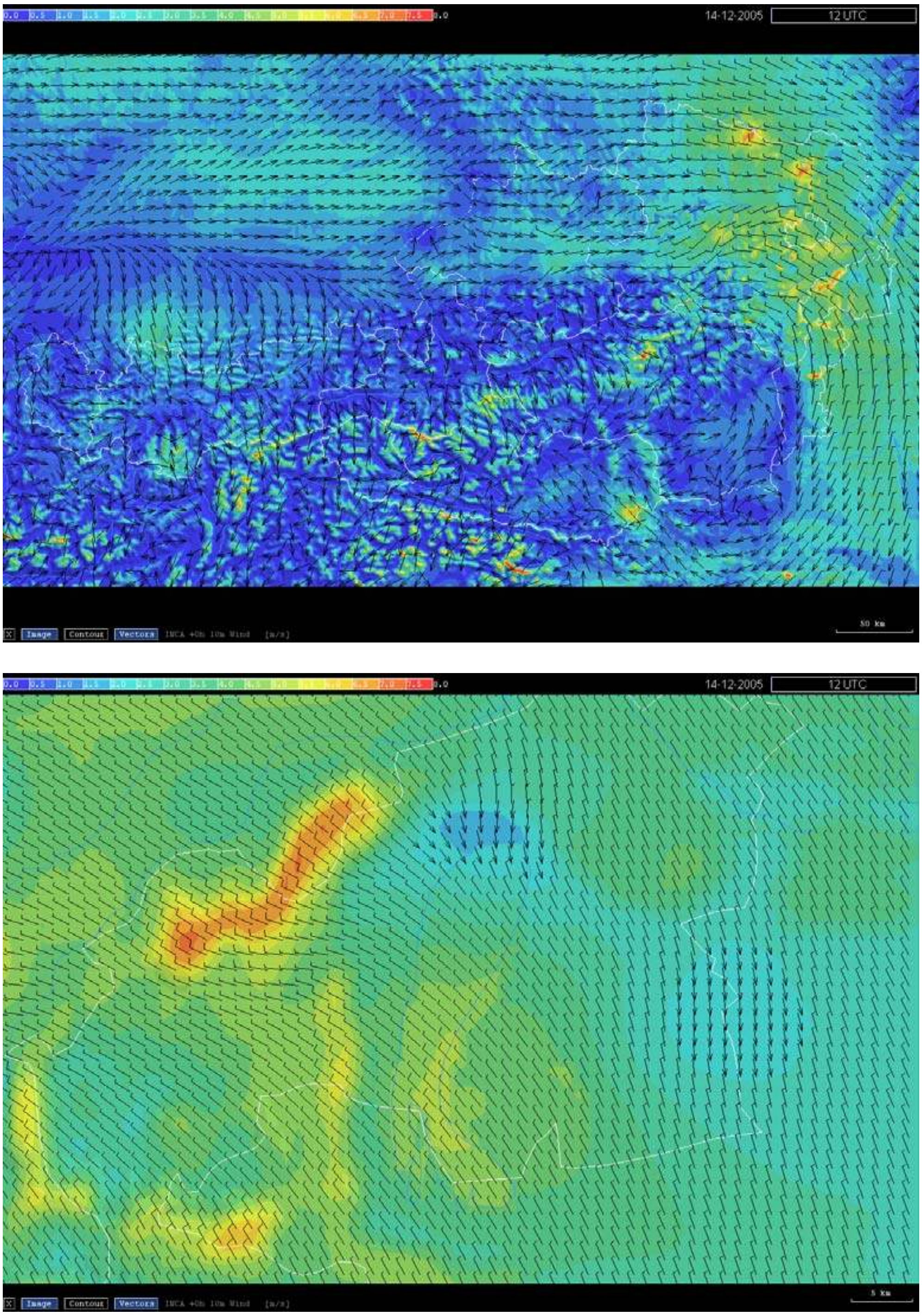

Figure 5.2.3: Example of a 10 m wind analysis provided by the INCA wind module. Colors give wind speed, wind vectors indicate direction and speed. Top: analysis for the entire INCA domain, bottom: zoom on the Lake Neusiedl area. Over the lake, analysed 10 m wind speeds are typically 10-20% higher due to the smaller roughness length over water computed with (5.2.2)-(5.2.5).

where the dependence of roughness length over water on wind speed is taken into account using Charnock's formula

$$z_0 = \frac{\alpha_c u_*^2}{g} \qquad (5.2.7)$$

with the nondimensional coefficient α_c =0.016 as suggested by Chamberlain (1983).

A future development in the INCA wind analysis will be to generate a flow-field which is not just kinematically but also dynamically consistent. For the simulation of thermally driven slope winds at high resolution it is crucial to include nonhydrostatic pressure perturbations (Haiden, 2003). With regard to katabatic flows it was shown by Haiden and Whiteman (2005) that significant mass-fluxes can be generated even on very gentle slopes with inclinations of the order of 1%.

5.3 Cloudiness

The cloudiness analysis in INCA is actually an analysis of insolation fraction S_P based on station observations, using MSG cloud type data for spatial interpolation. The approach is similar to the INCA precipitation analysis in the sense that no NWP model output is used in the analysis, and that remote sensing data is calibrated using station observations. Also, a certain spatial shift (5 km) between station location and satellite pixel is allowed in order to take into account uncertainties in timing and satellite imagery navigation as well as the slanted path of the sunbeam. The essential idea in the case of cloudiness is to perform spatial interpolations of station observations separately for each set of stations that is located beneath a certain cloud type. Thus the relationship between cloud type and insolation fraction on a given day does not get ‘smeared out’ in areas where different cloud types are bordering each other. On the resulting field some weak smoothing is applied, consistent with the amount of spatial shift between station and satellite pixel described above. Figure 5.3.1 shows how the cloud type information improves the spatial structure of the insolation fraction field compared to the typical bulls-eye structure obtained from station interpolation alone. During nighttime, when no station observations of equivalent ‘starlight’ fraction are available, the field is simply the cloud types themselves, scaled according to a one-year validation period. Thus, the cloud types are transformed into ‘starlight’ fraction on a monthly basis with linear temporal dependency in order to avoid discontinuities at month-end.

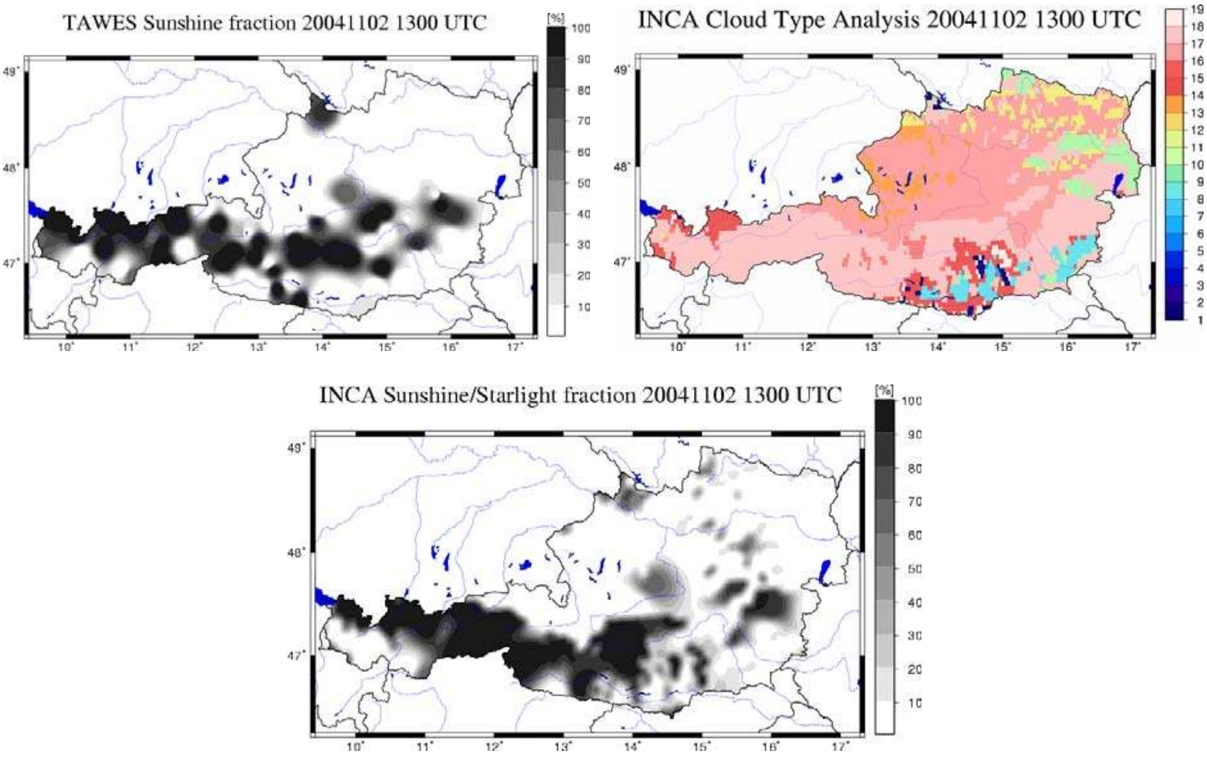

TAWES Sunshine fraction 20041102 1300 UTC

INCA Cloud Type Analysis 20041102 1300 UTC

INCA Sunshine/Starlight fraction 20041102 1300 UTC

Figure 5.3.1: Insolation fraction from station interpolation (upper left), MSG cloud types (upper right), and combined INCA insolation fraction analysis (bottom). [During the work on the project the parameter S_P was used for this field, meaning 'sunshine' percent. At night the equivalent field would have to be called 'starlight' percent, or fraction.]

5.4 Precipitation [inca_rr.c, rr_elev.c]

The precipitation analysis is a combination of station data interpolation including elevation effects, and radar data. It is designed to combine the strengths of both observation types, the accuracy of the point measurements and the spatial structure of the radar field. The radar can detect precipitating cells that do not hit a station. Station interpolation can provide a precipitation analysis in areas not accessible to the radar beam. Naturally, the combination method has to deal with the weaknesses of both types of observation as well, namely the potentially unrepresentative locations, and low density, of stations, and the fundamental quantitative uncertainty of precipitation estimated by radar.

(i) Interpolation of station data

The 1-min precipitation amounts measured at TAWES stations are aggregated to 15-min amounts. The irregular point values are interpolated onto the regular 1×1 km INCA grid using distance weighting. A common method of interpolation of point precipitation measurements onto a regular grid is based on weights that are the *n*-th power of inverse distance. It can be written

$$P_{STAT}(i,j) = \frac{\sum_k \frac{P_k}{r_{ijk}^n}}{\sum_k \frac{1}{r_{ijk}^n}}, \tag{5.4.1}$$

where

$$r_{ijk} = \sqrt{(x_k - x_i)^2 + (y_k - y_j)^2} \tag{5.4.2}$$

is the distance between station *k* and grid point (*i, j*), and P_k is the precipitation at station location *k*. Eqs. (5.4.1) and (5.4.2) produce a gridded precipitation field that reproduces (within the limits of grid resolution) the observed precipitation values at the station locations, and exhibits reasonably smooth behaviour in between. In regions that are far from any station, the field asymptotically approaches the station mean.

Often the exponent *n*=2 (inverse-distance-squared, IDS) is used for interpolation, which tends to generate precipitation bulls-eyes, in particular if the summation at each grid point is taken over all stations. This undesirable tendency may be alleviated by either performing the summation over a fixed number of nearest stations only (as in INCA), or by limiting the summation to stations within a certain radius. Alternatively, the exponent may be increased from 2 to a higher value, for instance to an inverse-distance-to-the-4th-power. Each of these modifications reduces the influence of distant stations and generates a precipitation field which is more locally determined, and more similar to what a human analysis made by hand would produce. Cross-validation studies during the initial development of INCA have shown that an exponent of 2 or even smaller produces the best analyses in the case of widespread rainfall, whereas significantly higher values (>5) are best suited for isolated convective events. Since the latter type of event is anyway captured by the radar data, the value 2 which is more suitable for widespread precipitation is used operationally. To reduce the occurrence of precipitation bulls-eyes, only the nearest 8 stations are taken into account in the interpolation. Furtermore, a modification to the classical IDS method has been introduced. It takes into account the inhomogeneous azimuthal distribution of stations around the gridpoint in question and reduces the relative weight of stations located ‘behind’ (i.e. at a similar azimuth to) nearer stations.

(ii) Climatological scaling of radar data

The radar data, which is available at 5 minute intervals on a polar-stereographic projection, is aggregated to 15-min precipitation amounts, and bilinearly interpolated onto the INCA grid. Let us denote this field by $P_{RADAR}(i,j)$. Since the radar field is strongly range-dependent and contains biases due to topographic shielding it must be scaled before use in the precipitation analysis. In a first step, a ’climatological’ scaling is performed. A climatological scaling factor $RFC(i,j)$ is calculated for each month. A gridded field of the scaling factor is obtained through interpolation of the scaling factors calculated at every station *k* as the ratio between monthly totals of raingauge and radar precipitation

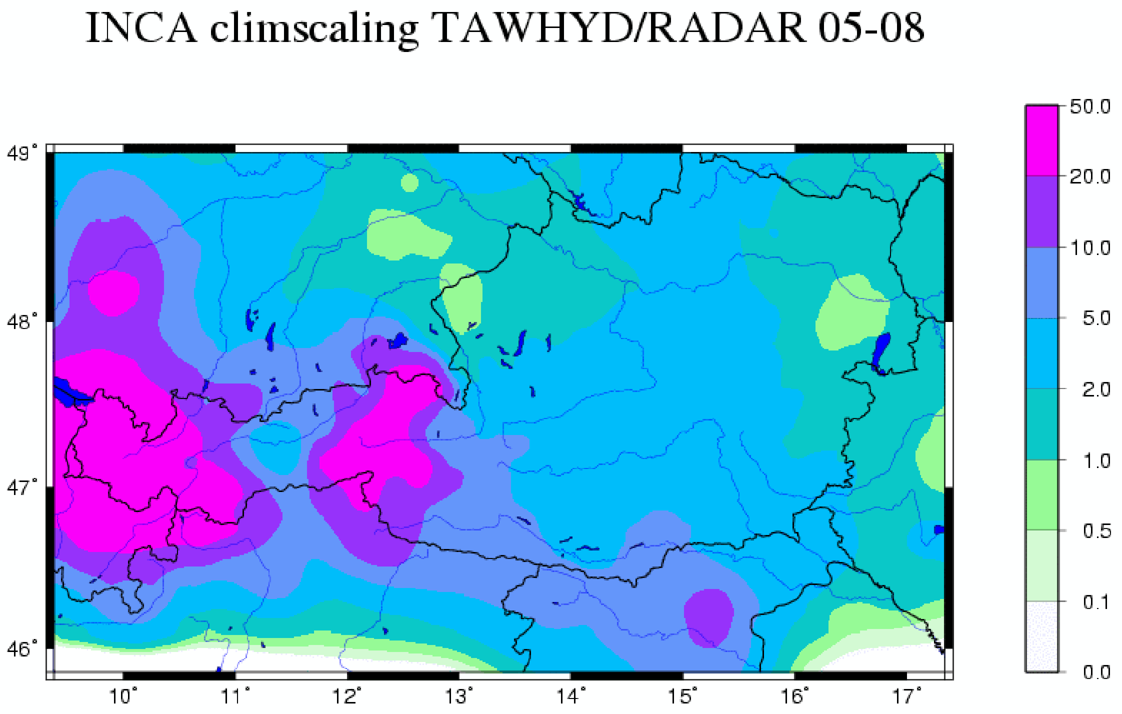

Figure 5.4.1: Climatological radar scaling factor derived as the ratio between raingauge and radar accumulated precipitation based on the convective season (May-August) 2005. It can be seen that large areas in Vorarlberg, Tyrol, and Salzburg exhibit very poor radar coverage (values of 10 and higher), whereas Upper and Lower Austria are satisfactorily covered, with values mostly between 1 and 3.

$$RFC_k = \frac{\sum_{month} P_k}{\sum_{month} P_{RADAR,k}} . \tag{5.4.3}$$

The resulting field (Figure 5.4.1) is spatially smoothed using a 10×10 km running average. Operationally, a 3-month temporal average of scaling factors centred at the actual month is used. This climatological scaling only partially corrects the reduced radar return in the case of snowfall as compared to rain.

In order to compensate for some of the artefacts in the radar field caused by topographic shielding of the radar beam, the interpolated scaling factor is replaced by a local scaling factor in regions where the radar beam is strongly shielded (indicated by beamlike structures with high local scaling factors). The local scaling factor is the ratio of the monthly accumulated precipitation gained from the interpolated station observations to the accumulated radar precipitation at the respective gridpoint:

$$RFC_l(i,j) = \frac{\sum\limits_{month} P_{STAT}(i,j)}{\sum\limits_{month} P_{RADAR}(i,j)} \tag{5.4.4}$$

Multiplication of the resulting scaling factor field $RFC(i,j)$ or $RFC_l(i,j)$ (whichever is higher) with the radar field yields the climatologically adjusted radar field

$$P^*_{RADAR}(i,j) = \max\left[RFC(i,j), RFC_l(i,j)\right] P_{RADAR}(i,j)\,. \tag{5.4.5}$$

Below, whenever RFC occurs in an equation, it is the maximum of RFC and RFC_l that is actually used.

There are two kinds of problems with this scaling procedure. The first are regions where the radar field is very weak or nonexistent because the radar beam is shielded by mountains. In these regions simple scaling would yield arbitrarily high scaling factors resulting in questionable precipitation values. This undesirable effect is prevented by limiting the scaling factor to a maximum value RFC_CR (currently set to 2). The second problem is that high precipitation rates, typically found within convective cells, are more visible and thus less underestimated by radar. To prevent over-scaling of such cells the scaling factor is reduced for radar values higher than RR_CR (currently set to 1 mm / 15 min) in the form

$$RFC_{RED}(i,j) = 1 + [RFC(i,j) - 1]\frac{RR\_CR}{P_{RADAR}(i,j)} \tag{5.4.6}$$

[climscale_RR()]. Thus the scaling factor asymptotically decreases towards 1 for high precipitation amounts.

(iii) Re-scaling of radar data using the latest observations

In a next step the climatologically scaled radar field is re-scaled on the basis of a comparison at analysis time of station observations and radar values at the stations. In this comparison, a spatial shift of a maximum of 4 km in either direction between the station and the corresponding radar pixel is allowed to take into account effects due to the finite settling time of hydrometeors, effects of wind-drift, etc. The algorithm identifies the radar pixel that fits best to the station observation, and uses that value for subsequent calculations. An optimum spatial shift vector is computed for each station location and interpolated to each grid point with a distance-weighting algorithm. Using this shift-vector field, the radar precipitation field is shifted at each grid point in a slightly different direction and amount [shift_RR()].

The actual re-scaling [rescale_RR()] has the form

$$P_{RADAR}^{**}(i,j) = \frac{\sum_k w_{ijk} RFA_{ijk}}{\sum_k w_{ijk}} P_{RADAR}^{*}(i,j) \,. \tag{5.4.7}$$

It is nonlinear because the weights w_{ijk} and the scaling factor RFA_{ijk} depend on $P_{RADAR}^{*}(i,j)$. The weights have the form

$$w_{ijk} = \frac{\min\left(1, \frac{P_{RADAR,k}^{*}}{P_{RADAR}^{*}(i,j)}\right)}{r_{ijk}^2 + \left[c\left(RFC_k - RFC(i,j)\right)\right]^2} \,, \tag{5.4.8}$$

where r_{ijk} is the geometric distance given by (5.4.2). Compared to inverse distance weighting, (5.4.8) contains two additional terms. The additional term in the denominator increases the distance if the climatological scaling factor at a station and at the point in question are different. The coefficient has the value *c*=10 km, which means that a difference in scaling factors of 1 has the effect of a distance increase by 10 km. This term is important especially in mountain areas, where the *RFC* field can vary considerably over short distances due to topographic shading. The term in the numerator reduces the weight if the radar precipitation value at a station is smaller than the one at the point in question.
The scaling factor RFA_{ijk} in (5.4.7) is given by

$$RFA_{ijk} = \min\left(RFA^{+}(i,j), \frac{P_{STAT,k}}{P_{RADAR,k}^{*}}\right), \tag{5.4.9}$$

where the parameter RFA^{+} is a function of the climatological scaling at the gridpoint in question

$$RFA^{+}(i,j) = \min\left[RFA_{MAX}, \max\left(RFA_{MIN}, RFC_P - RFC(i,j)\right)\right], \tag{5.4.10}$$

with RFA_{MIN}=1, RFA_{MAX}=3, RFC_P=5. In summary, the scaling defined by (5.4.7)-(5.4.10) for a gridpoint (*i,j*) is a weighted average of the ratio between station and radar precipitation at the nearest stations, where the weight decreases with increasing distance, with increasing difference in climatological scaling, and with decreasing precipitation at the station (relative to the precipitation at the gridpoint).

(iv) Final combination

The two precipitation fields $P_{STAT}(i,j)$ and $P_{RADAR}^{**}(i,j)$ are finally combined to a field $P_{INCA}(i,j)$ that gives a better estimate of the precipitation distribution than each individual field. The combination is obtained through a weighting relationship

$$P_{INCA}(i,j) = P_{STAT}(i,j) + v\left[P_{RADAR}^{**}(i,j) - P_{RADSTAT}^{**}(i,j)\right] \,, \tag{5.4.11}$$

[create_RM()] where the weight *v* is given by

$$v(i,j)=\begin{cases} 1 & RFC < RFC_0 \\ \exp\left[-\ln(2)\left(\dfrac{RFC-RFC_0}{RFC_H-RFC_0}\right)^2\right] & RFC \geq RFC_0 \end{cases}. \qquad (5.4.12)$$

The auxiliary field $P^{**}_{RADSTAT}(i,j)$ is created by interpolating onto the grid, analogous to the station observations, the scaled radar values at the station locations. At the station locations $P^{**}_{RADAR}(i,j)=P^{**}_{RADSTAT}(i,j)$, so that *v*=0, and the station observations are reproduced there within the limits of resolution. Between the stations, the weight of the radar information becomes larger the better the radar captures the precipitation climatologically, i.e. the smaller the *RFC* values are. The threshold value RFC_0, above which the weight of the radar begins to decrease, is 3. The value of RFC_H, at which the radar weight has decreased to one-half, is 5.

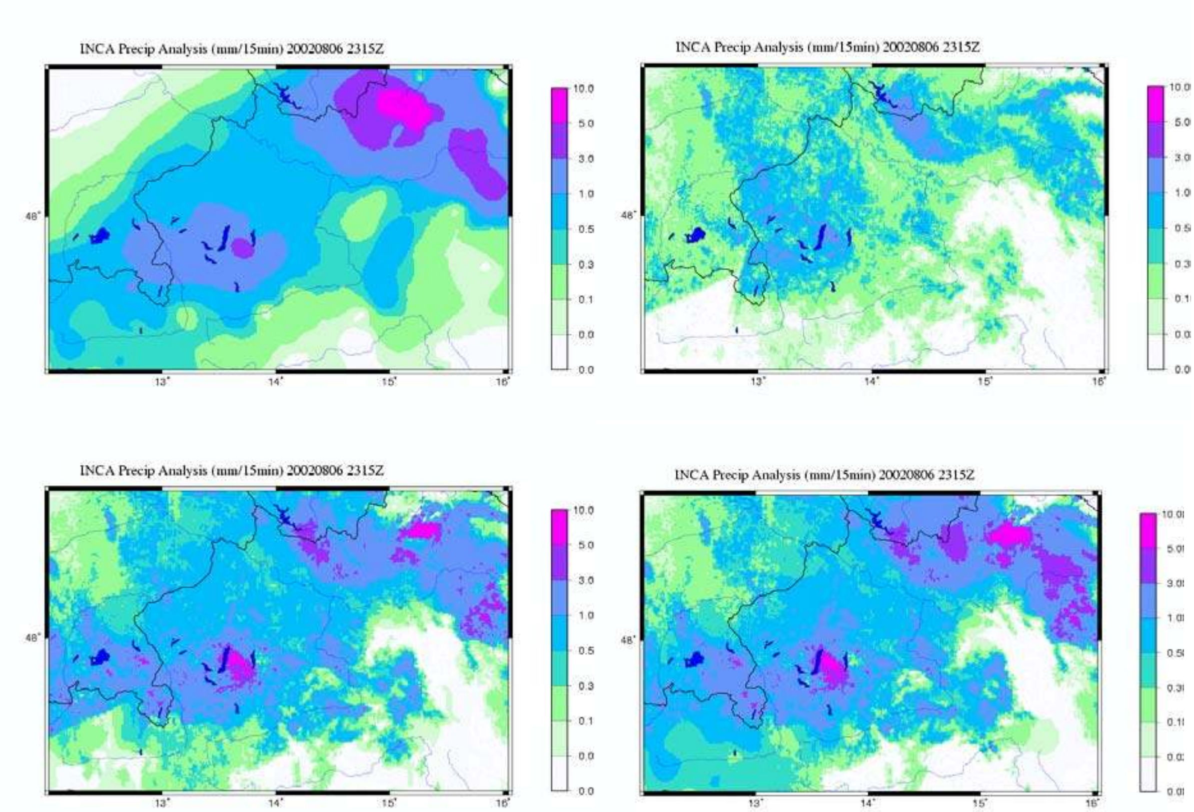

Figure 5.4.2: Example of a 15-min INCA precipitation analysis based on the combination of station and radar data. Upper left panel: pure station interpolation, upper right panel: uncorrected radar field, bottom left panel: corrected radar field, bottom right panel: final INCA precipitation analysis.

Figure 5.4.2 shows an example of the stepwise procedure and final analysis from the 2002 flood event in Austria. Note the large difference between unscaled radar and station interpolation (top panels), and the importance of the final combination (lower right panel) as a means to smoothly connect areas seen by radar with those only covered by stations. If the final combination step is not made, ‘edges’ would remain in the analysis (lower left panel, SW corner).

(v) Elevation dependence

A new feature introduced in 2008 was a parameterization of elevation effects on precipitation. They were found to be crucial for a realistic estimation of the spatial distribution of precipitation in mountainous terrain. Through feedback from hydrological simulations using INCA precipitation analyses it was possible to constrain and optimize the parameterization.

In the study of elevation effects on precipitation it is necessary to define the spatial scale at which the relationship is supposed to be valid. In the Alpine area no systematic increase of precipitation with elevation exists on the 50-100 km scale. Precipitation increases from the Alpine foreland towards the northern and southern upslope areas and generally decreases towards the interior Alpine areas, in spite of higher terrain there (Frei and Schär 1998). These areas experience precipitation shielding due to mountain-range blocking and upslope effects. This is a familiar pattern that can be found in many other areas such as the Pacific coastal mountains of the U.S. and Canada, or the mountains of Norway and Sweden. However, superimposed on this larger scale are patterns due to individual mountain ridges and valleys (5-10 km scale). It is the variation on this horizontal scale we attempt to parameterize. It also appears to be the optimal scale for the application of elevation-precipitation relationships (Daly et al. 1994, Sharples et al. 2005). Moreover, the average distance between real-time rain gauge stations in the Austrian Alps is ~20 km which means they already capture most of the meso-β scale precipitation variations. This is another reason why our study focuses on the local (5-10 km) meso-γ scale increase of precipitation from a valley floor to the surrounding ridges and peaks.

Table 5.4.1: Topographic characteristics of station pairs used in the analysis. The last column gives the direction of the valley station relative to the mountain station.

#	Station	z(m)	Δz(m)	Δx(m)	Dir
1	Hahnenkamm Kitzbühel	1790 744	1046	3800	NNE
2	Loferer Alm Lofer	1623 625	998	4200	ESE
3	Schmittenhöhe Zell am See	1973 766	1207	4400	E
4	Feuerkogel Gmunden	1618 427	1191	4300	E
5	Rax Reichenau	1547 486	1061	4900	ESE

Table 5.4.1 lists the station pairs used for the derivation of the parameterization. The horizontal distance between mountain and valley stations is about 4 km, the vertical distance is about 1 km. On the meso-β scale, station pairs 2 and 4 are located in the primary northern Alpine upslope precipitation belt, whereas station pairs 1, 3, and 5 are experiencing already some downstream sheltering. Pairs 1-4 are located well north of the main Alpine crest, pair 5 is situated at the eastern end of the Alpine chain. For this study we used 12-h precipitation observations (06-18 UTC, 18-06 UTC) from the 11-yr period 1995-2005. The observations were corrected for wind effects following the method of Skoda and Filipovic (2007) which

estimates a correction factor as a function of precipitation intensity, wind speed, and wet-bulb temperature (for the distinction between snow and rain).

The parameterization derived from these station pairs gives the mountain precipitation as a function of valley precipitation, normalized to a height difference of 1000 m. It has the form

$$P_{mtn} = \begin{cases} P_{val}(a - bP_{val}) & P_{val} \le P_c \\ P_{val} + (a - 1 - bP_c)P_c & P_{val} \ge P_c \end{cases}, \tag{5.4.13}$$

where $P_c = (a-1)/(2b)$. Alternatively, (5.4.13) can be written

$$P_{mtn} = \begin{cases} P_{val}\left[1 + (a-1)\left(1 - \dfrac{P_{val}}{2P_c}\right)\right] & P_{val} \le P_c \\ P_{val} + \dfrac{a-1}{2}P_c & P_{val} \ge P_c \end{cases}, \tag{5.4.13'}$$

[g_oro_fun()] where b has been expressed in terms of a and P_c (Haiden and Pistotnik 2008, 2009). The parameter a is the ratio between mountain and valley precipitation in the limit of weak valley precipitation. The parameter b is a measure of how strongly the ratio between mountain and valley precipitation decreases with increasing valley precipitation. For small values of valley precipitation, (5.4.13) reduces to the simple linear relationship

$$P_{mtn} = aP_{val}. \tag{5.4.14}$$

As P_{val} increases, but remains below the critical value P_c, the ratio P_{mtn} / P_{val} decreases, and mountain precipitation as given by (5.4.13) becomes a parabolic function of valley precipitation. Above the critical value, the relationship between P_{val} and P_{mtn} is additive. For a given value of the parameter a, an optimum value of b is computed from a given ratio of long-term (inter-annual) precipitation totals at the mountain and valley stations

$$A = \frac{(P_{mtn})_{ann}}{(P_{val})_{ann}} \tag{5.4.15}$$

by minimizing the mountain precipitation root-mean-square error (RMSE) when predicted by valley precipitation. Note that the numbers given below all refer to values of A, a, b normalized to an elevation difference of 1000 m between mountain and valley station.

The different behaviour of orographic precipitation enhancement in the limit of small and high precipitation rates implied by (5.4.13) is consistent with the physics of the seeder-feeder process (Smith 1979, Cotton and Anthes 1989). If the non-orographic (seeding) precipitation is weak (Fig. 5.4.3a), orographic enhancement is limited by conversion. Only a small fraction of the condensate produced in the orographic cloud is washed out. Increasing the seeding therefore leads to a roughly proportional increase of precipitation at the ground. If the seeding rate is high (Fig. 5.4.3b), washout of condensate is very efficient, and orographic enhancement becomes limited by condensation. An increase in the intensity of seeding does not lead to a proportional increase of precipitation at the ground. The orographic effect is basically additive in such a case. As shown analytically by Haiden (1995), the critical seeding rate, above which the process becomes limited by condensation rather than accretion efficiency, increases with wind speed.

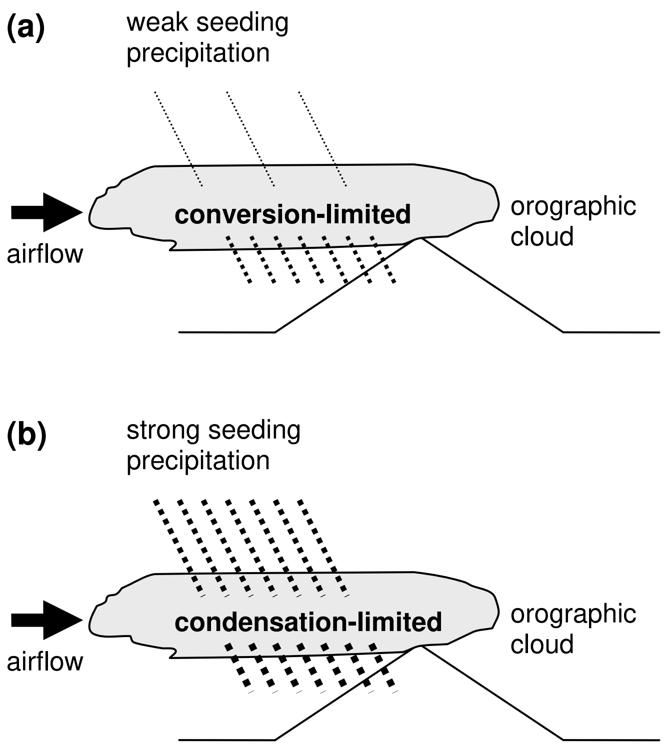

Figure 5.4.3: If the non-orographic (seeding) precipitation is weak (a), orographic enhancement is limited by conversion. If seeding is strong (b), orographic enhancement is limited by condensation.

It was found that the coefficient a, which represents the precipitation enhancement for small precipitation amounts, could be set to the location-independent value of 2.2 without significantly increasing the RMSE. We applied (5.4.13) with a=2.2 to the 11-yr dataset, varying the coefficient b, thereby obtaining different inter-annual ratios A. The relationship between A and b is quite similar for all 5 station pairs, confirming the viability of the general approach. The similarity appears to be a result of the broadly similar precipitation climate at the selected locations. The relationship can be analytically fitted by

$$b(A) = \frac{1}{c_1(A-1)} - \frac{1}{c_2}, \tag{5.4.16}$$

where c_1 = 16.0 mm and c_2 =18.6 mm (12-h totals).

The actual implementation of the elevation parameterization works as follows. In a first step, a 'station topography' $z_{ST}(i,j)$ is created. It is the topography represented by the stations and is computed by interpolating the INCA elevation at the station locations

$$z_{ST}(i,j) = \frac{\sum_k \frac{z_{H,k}}{r_{ijk}^2}}{\sum_k \frac{1}{r_{ijk}^2}}, \tag{5.4.17}$$

where r_{ijk}^2 is given by (5.4.2). Similarly, a 'valley precipitation' field is computed

$$P_{VAL}(i,j) = \frac{\sum_k \frac{P_k}{r_{ijk}^2}}{\sum_k \frac{1}{r_{ijk}^2}} \qquad z_k - z_{V,k} \le \Delta z_{VAL}, \tag{5.4.18}$$

where the summation extends only over those stations which are located not more than Δz_{VAL}=300 m above the valley floor surface. The field P_{VAL} represents the reference precipitation at valley floor level, on which the elevation dependence is based. In the following, we drop the (*i,j*) arguments for better legibility, where it is understood that each dependent variable is a gridded field depending on (*i,j*).

The relationship (5.4.13) between mountain and valley precipitation, which was normalized to a height difference of 1000 m, implies a certain relative precipitation gradient

$$G_{ELEV} \equiv \frac{1}{P}\frac{\Delta P}{\Delta z} \approx \frac{1}{P_{VAL}}\frac{P_{MTN} - P_{VAL}}{\Delta z} = \frac{1}{\Delta z}\left(\frac{P_{MTN}}{P_{VAL}} - 1\right). \tag{5.4.19}$$

Using (5.4.13), (5.4.16), and (5.4.19), the precipitation increment due to the elevation effect on the INCA grid is computed from

$$\Delta P_{ELEV} = G_{ELEV}(\hat{z}_H - z_{ST})P_{VAL}, \tag{5.4.20}$$

where the modified topography height $\hat{z}_H$, defined by

$$\hat{z}_H = \begin{cases} Z_{MAX} - \Delta Z \exp\left(-\frac{z_H - Z_{MAX} + \Delta Z}{\Delta Z}\right) & z_H > Z_{MAX} - \Delta Z \\ z_H & z_H \le Z_{MAX} - \Delta Z \end{cases}, \tag{5.4.21}$$

has been introduced to reduce the elevation gradient at higher elevations. For Austria, parameters values have been set to Z_{MAX}=2800 m, and ΔZ=500 m.

Finally, the increments due to radar field and elevation dependence need to be combined. Eq. (5.4.11) can be written

$$P_{INCA} = P_{STAT} + \Delta P_{RADAR}, \tag{5.4.22}$$

where

$$\Delta P_{RADAR} \equiv v\left(P_{RADAR}^{**} - P_{RADSTAT}^{**}\right). \tag{5.4.23}$$

To avoid double counting of elevation effects already captured by the radar field, the combination is additive only if the increments have different sign

$$\Delta P = \Delta P_{RADAR} + \Delta P_{ELEV} \qquad \text{if} \qquad \Delta P_{RADAR} \cdot \Delta P_{ELEV} < 0, \tag{5.4.24a}$$

and if they have the same sign, then just the larger value is used

$$\Delta P = \max\left(\Delta P_{RADAR}, \Delta P_{ELEV}\right) \qquad \text{if} \qquad \Delta P_{RADAR} \cdot \Delta P_{ELEV} \ge 0. \tag{5.4.24b}$$

Eq. (5.4.22) is replaced by

$$P_{INCA} = P_{STAT} + \Delta P \ , \tag{5.4.25}$$

where ΔP now contains both radar and elevation increments [oro_effect()].

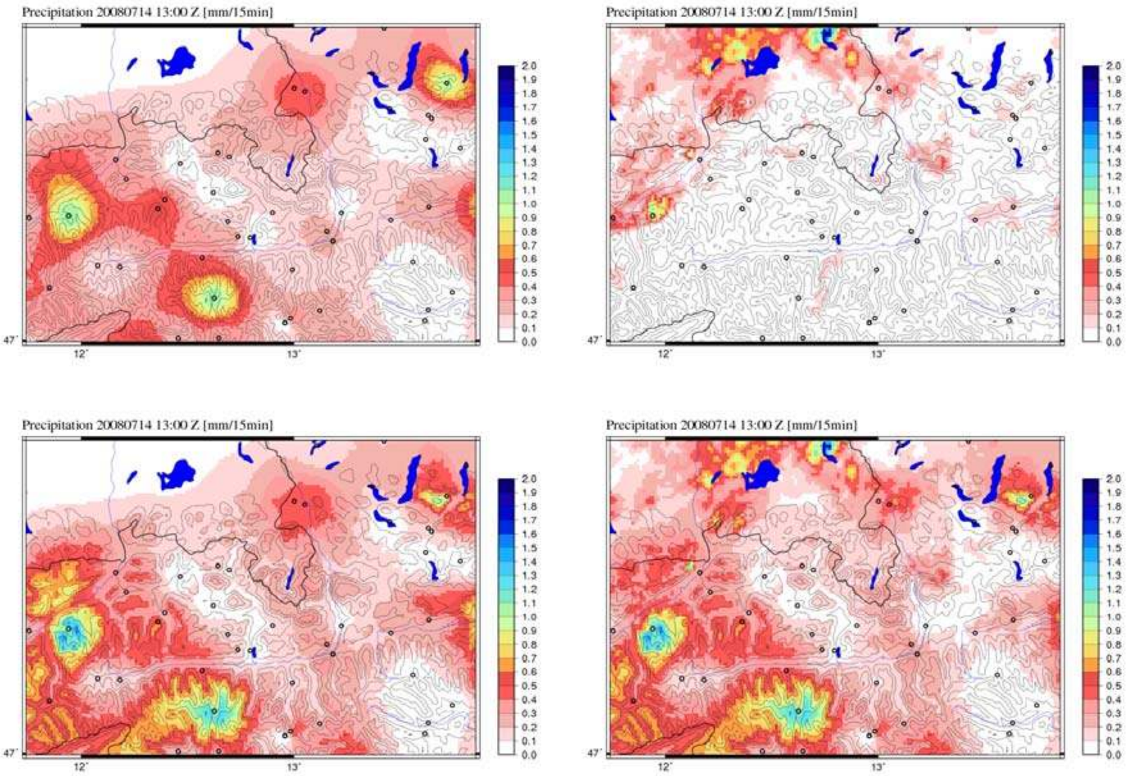

Figure 5.4.3: Example of a 15-min INCA precipitation analysis based on the combination of station and radar data, with elevation dependence included. Upper left panel: pure station interpolation, upper right panel: radar field, bottom left panel: station interpolation with elevation effect, bottom right panel: final INCA precipitation analysis.

5.5 Precipitation type

The ALADIN model provides forecasts of liquid and solid precipitation at the height of the model topography. This information is however of limited use in orographically structured terrain, where the model topography may differ greatly from the actual topography. For the city of Innsbruck, for example, which is located at about 600 m above msl, the current ALADIN-AUSTRIA model topography has a height of 1500 m, giving a difference in elevation of 900 m. In several alpine valleys these differences reach values of up to 1500 m. Using a semi-envelope or mean orography instead of the full envelope reduces these differences but does not eliminate the problem of predicting the actual snowfall line in terrain that is only partially resolved by a model. This is an issue in flood forecasting, where the amount of precipitation stored as snow on the ground (thus not immediately contributing to runoff) needs to be estimated. It is also crucial in road weather forecasts for the planning of road maintenance measures like plowing and salting.

Furthermore, for such applications the distinction between rain and snow may not be sufficient. In cases where the atmosphere is well-mixed, and the temperature continuously decreases with height, the boundary between snowfall and rainfall will be relatively narrow. However, in more stable cases, or when the snowfall line works its way downwards due to latent heat effects, there may be a broader height range with temperatures close to 0°C and associated snow/rain mix ('Schneeregen'). If rain falls into a near-surface layer of cold air, or on a surface with sub-freezing temperature, freezing rain will occur. This precipitation type is the most critical of all since it has enormous effects on transportation and may cause widespread structural damage in severe cases (Rauber et al., 1994).

One of the derived fields from ALADIN-AUSTRIA we operationally compute outside the model is the snowfall line. The distinction between rain and snow is based on wet-bulb temperature T_w rather than temperature T because ventilation effects keep the temperature of falling precipitation close to T_w. It is well known that snowfall may occur at several degrees above 0°C if the atmosphere is sufficiently dry. Steinacker (1983) has shown empirically that the threshold value of T_w for the rain/snow distinction is close to $(T_w)_{crit} = +1.5$°C. This is the value we use in the computation of ALADIN snowfall line.

The ALADIN forecast of temperature T and specific humidity q on pressure levels is interpolated to the INCA grid and extrapolated into valleys as described in Section 5.1. Next, starting from the top, T_w is computed at each level, marching downward. When the first $T_w > (T_w)_{crit}$ is found, the height of the snowfall line is computed from linear interpolation between this level and the one above. Since there is no closed analytical expression for $T_w = f(T, q, p)$ the computation is iterative, using a bisection algorithm. In cases where the snowfall line is below the lowest terrain elevations, it is set to a default value.

The determination of precipitation type is also based on the wet-bulb temperature. According to the observational study of Steinacker (1983) a snow/rain mix is most likely to occur in the range 0°C $\leq T_w \leq$ +2°C. Below 0°C precipitation predominantly falls as pure snow, and above +2°C it is most likely pure rain. [Thus the snowfall line as described above actually represents a specific height within the finite-thickness melting layer.] Because of the potentially complicated vertical temperature and humidity structure in the lower atmosphere, it is not sufficient to just rely on near-surface values. For example, even if $T_w <$ 0°C, theoretically allowing pure snowfall, there may be a warm layer aloft where the precipitation has already completely melted and it actually rains. The algorithm which determines precipitation type therefore uses both near-surface information (2m temperature, 2m wet-bulb temperature, ground temperature) and upper-air information (snowfall line as determined above).

1) $T_w <$ +2°C. If this is the case, the relation between snowfall line z_s and surface elevation z is considered. If $z_s - z < -1.5\,\Delta z_{melt}$, snowfall is diagnosed, if $-1.5\,\Delta z_{melt} < z_s - z < 0.5\,\Delta z_{melt}$, snow/rain mix, and if $z_s - z \geq 0.5\,\Delta z_{melt}$ rainfall.
2) $T_w \geq$ +2°C. Rainfall is diagnosed.

The value of $(\Delta z)_{melt}$ which represents the half-width of the melting layer, is currently set to a constant value of 100 m but will soon be replaced by the actual melting layer half-width computed from the thresholds $T_w =$ 0°C and $T_w =$ +2°C.

In cases where the above diagnosis gives rainfall, an additional test for freezing rain is performed. Freezing rain is assumed to occur if either the air temperature or the ground temperature is below 0°C. In the latter case, however, the air temperature must not exceed a critical value which is currently set to +2°C. In order to clarify whether this additional 'safety precaution' is really necessary, future freezing rain events will have to be analyzed. The analysis of ground temperature in INCA is based on surface observations of +5cm air temperature, –10cm soil temperature, and 2m air temperature. In its current version it is only used for the determination of freezing rain potential. Outside the nowcasting range, the ALADIN forecast of ground surface temperature is used (adapted to actual terrain height).

The computations described above have been operationally implemented in INCA which performs a precipitation analysis every 15 minutes. Since temperature, humidity, and ground temperature are updated only every 1 hour, a linear interpolation in time is used to provide an update on precipitation type every 15 minutes. The example in Figure 2 shows an analysis where all four precipitation types are present.

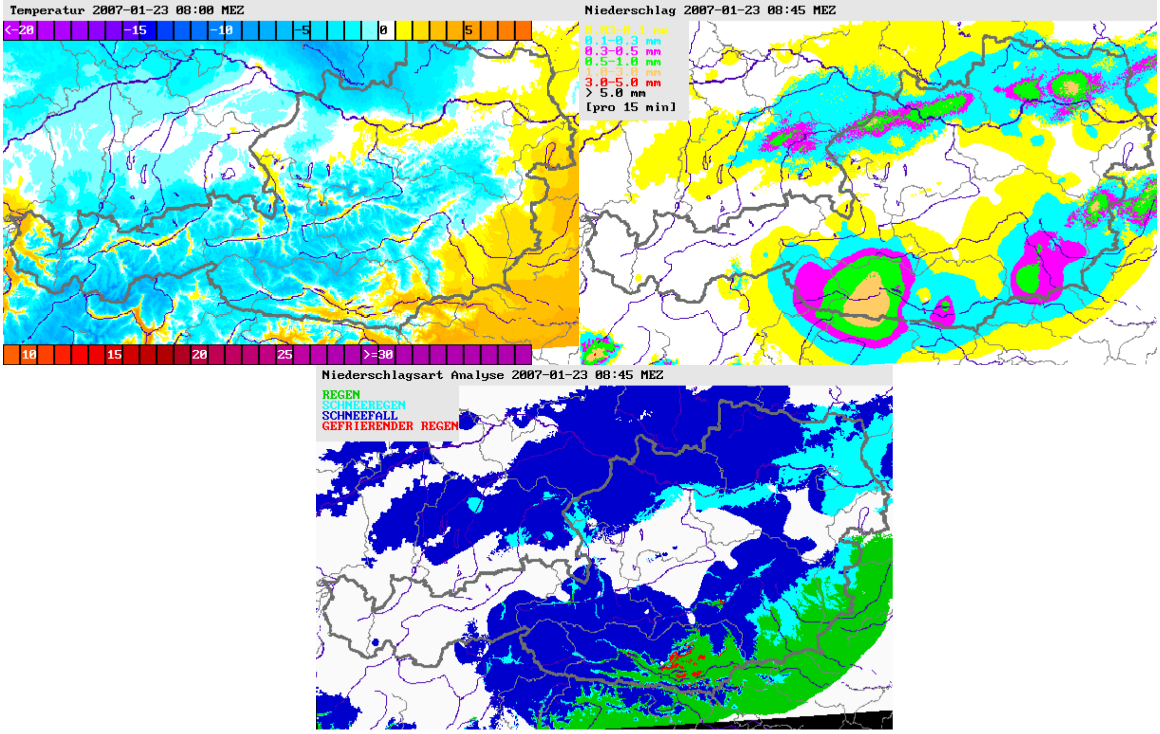

Figure 5.5.1: Example of an INCA analysis of temperature (upper left), precipitation (upper right), and resulting precipitation type (bottom). Snowfall indicated blue, snow/rain mix is light blue, rain is green, freezing rain is red. In this case freezing rain is diagnosed in some cold air pools which are present in inner-alpine basins. The temperature analysis is based on ALADIN as a first guess.

The current algorithm gives satisfactory results with regard to the distinction between snow, snow/rain mix, and rain, and there are indications that it gives useful guidance on the occurrence of freezing rain. However, since its full operational implementation no major freezing rain event occurred in Austria, so this still needs to be verified.

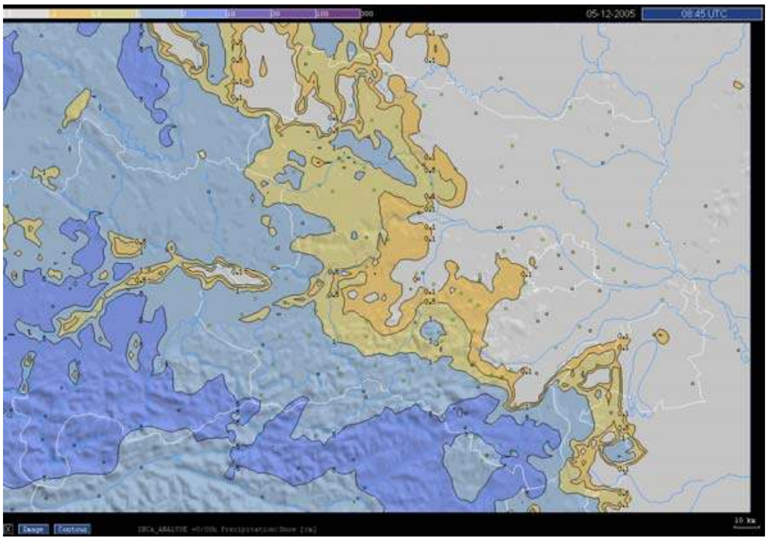

Figure 5.5.2: Example of an INCA snowfall analysis (in cm) generated from consecutive 15-min analyses accumulated over 8 hours. Shown is a zoom over northeastern Austria.

At gridpoints located above the local snowfall line, the accumulation of snow is estimated by simply assuming 1 mm precipitation = 1 cm of snow. An example is shown in Figure 5.5.2. The increase of snow depth, for a given water equivalent, with decreasing temperature is not taken into account. This is because the settling of the snowpack under its own weight is not modelled either, and the two effects partially compensate. An algorithm taking into account both effects will probably be implemented in 2007.

6. The INCA forecasting system

At the time of this writing the INCA forecasting system consists of separate modules for temperature/humidity, wind, cloudiness, and precipitation, using different methods of extrapolation in time. It is planned to replace these modules in the future by a unified nowcasting method based on the concept of error motion vectors (Section 7).

6.1 Temperature and humidity

The currently used method of predicting temperature in the nowcasting range has been adopted from a single-point application and treats each gridpoint independently. It makes certain assumptions about the persistence of the NWP forecast error, depending on stratification and cloudiness.

Much of the temperature error in the NWP forecast is due to errors in the cloudiness forecast and associated errors in the surface energy budget. If the model underestimates cloudiness, the predicted diurnal temperature evolution will likely be overestimating the actual one, and vice versa. It is assumed that the factor f_T of the diurnal amplitude reduction can be approximately related to the error C_{ERR} of cloud fraction through a linear relationship of the form

$$f_T = 1 + c_N C_{ERR} \tag{6.1.1}$$

where the coefficient c_N is typically found to be in the range 0.5-0.7. The temperature nowcast for time t_i is then computed from the recursive relationship

$$T_{INCA}(t_i) = T_{INCA}(t_{i-1}) + f_T \left[T_{ALADIN}(t_i) - T_{ALADIN}(t_{i-1}) \right] \tag{6.1.2}$$

where $T_{INCA}(t_0)$ is the temperature at the analysis time, determined by the method described in Section 5a. Thus the temperature forecast consists of the observed temperature plus the temperature change predicted by the NWP forecast, multiplied by a factor which depends on the cloudiness forecast error of the NWP model. If there is no cloudiness forecast error, the predicted temperature change is equal to the one predicted by the NWP model.

The temperature computed by (6.1.1)-(6.1.2) does not generally converge towards the ALADIN forecast at large lead times. Therefore the forecast is replaced by a weighted mean between the temperature given by (6.1.2) and the ALADIN temperature forecast for times $t_i > \tau_C$ in the form of a negative-exponential asymptotic approach.

$$T^*_{INCA}(t_i) = g\, T_{INCA}(t_i) + (1-g) T_{ALADIN}(t_i) \tag{6.1.3}$$

where

$$g(t_i) = \exp\left(-\frac{t_i - \tau_C}{\tau_D} \right). \tag{6.1.4}$$

The time scale τ_C depends on static stability, specifically on the presence and strength of inversions. If no inversion is present, τ_C =3 hours, if a strong inversion exists, it can reach values of up to 12 hours. This dependency accounts for observed variations in persistence of temperature forecast errors under different synoptic conditions. During wintertime, a typical situation with a high τ_C value is anticyclonic weather with a lifted inversion below which low stratus persists for several days. The scaling parameter τ_D is set to the constant value of 6 hours. Figure 6.1.1 illustrates the amount of forecast improvement obtained from the scheme.

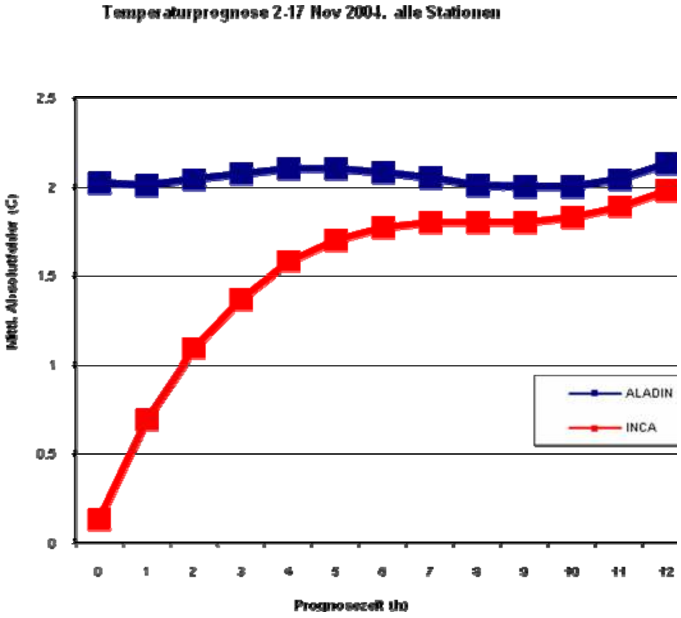

Figure 6.1.1: Mean absolute error of ALADIN and INCA temperature forecasts at lead times of +00 to +12 hours over a 2-week period in winter, for all TAWES stations. The improvement due the nowcasting scheme is most significant during the first 6 hours. The smaller error of the INCA forecast at larger lead times is mainly due to the more sophisticated downward temperature extrapolation in deep valleys.

6.2 Wind

As in the case of temperature and humidity, the wind forecast in INCA takes into account only the local NWP error, and merges into the NWP forecast according to a prescribed weighting function which decreases linearly from 1 to 0 in the interval between +0 and +6 hours. Thus the INCA forecast of the three-dimensional wind vector can be written

$$\vec{v}_{INCA}(t_i) = g\,\vec{v}_{INCA}(t_0) + (1-g)\,\vec{v}_{ALADIN}(t_i)\,, \tag{6.2.1}$$

where the weight function is given by

$$g(t_i) = \max\left(1 - \frac{t_i}{\tau_v}, 0\right), \tag{6.2.2}$$

with $\tau_v = 6$ hours. The reduced roughness over lakes is taken into account in the forecast using Eqs. (5.2.2)-(5.2.5), i.e. analogous to the method used in the analysis (Section 5.2).

6.3 Cloudiness

INCA nowcasts of cloudiness, or rather, insolation fraction *SP*, are based on cloud motion vectors derived from consecutive visible (during daytime) and infrared (during nighttime) satellite images. During sunrise and sunset, a time-weighted combination of both vector fields is used. The extrapolation is performed for a forecast range of up to +6 hours using a 15 min timestep. Special care must be taken at the boundaries of the INCA domain, where information is advected from outside. This is done by extrapolation of Cloud Types that are generated with IR cloud motion vectors. The advected cloud type is then transformed to the corresponding cloudiness parameter by spatial and temporal adjustment using the information of the recent time step. Applying some weak filtering finally reduces inhomogeneities at the transition zone of extrapolated insolation fraction and extrapolated cloud types that are post-converted into insolation fraction. The nowcasting procedure of cloudiness is finalized by a consistency check with the nowcasting field of precipitation.

The NWP model (ALADIN) forecast of low, medium, and high cloudiness is converted to an insolation fraction forecast SP_{ALADIN} using the empirical relationship

$$SP_{ALADIN} = 1 - (c_l C_{low} + c_m C_{med} + c_h C_{high}) \tag{6.3.1}$$

with coefficients $c_l = 1.0, c_m = 0.65, c_h = 0.35$. The resulting insolation fraction field SP_{ALADIN} is interpolated onto the INCA grid and combined with the extrapolated field SP_{EXTRAP}. In order to perform forecasts with a range of 48 hours, an insolation fraction field SP_{ECMWF}, taken from ECMWF, which is created in the same way as SP_{ALADIN}, is used for the combined field SP_{PSEUDO_OPT}. Avoiding inhomogeneities, a time-weighted, smooth transition is performed. Analogous to precipitation, a smooth transition from the extrapolation forecast to the NWP forecast is constructed through a prescribed weighting function. The current operational weighting function gives full weight to the extrapolation forecast over the first 2 hours, decreases linearly to zero at 6 hours, and remains at zero beyond 6 hours. Thus the INCA forecast of insolation fraction can be written

$$SP_{INCA}(t_i) = g\, SP_{EXTRAP}(t_i) + (1-g)\, SP_{PSEUDO\_OPT}(t_i)\,, \tag{6.3.2}$$

where the weight function is given by

$$g(t_i) = \max\left(\min\left(1 - \frac{t_i - \tau_{c1}}{\tau_{c2} - \tau_{c1}}, 1\right), 0\right), \tag{6.3.3}$$

with $\tau_{c1} = 2$ hours, $\tau_{c2} = 6$ hours.

Figure 6.3.1 shows the analysis of insolation fraction *SP* for 20060117 0930Z. The corresponding motion vectors (Figure 6.3.2) are obtained from consecutive visible satellite images. They are averaged over one hour in order to reduce random fluctuations generated by pseudocorrelations. Extrapolation of the *SP* analysis up to +120min produces the *SP* nowcast shown in Figure 6.3.3. For comparison, the verifying *SP* analysis field at 20060117 1130Z is displayed in Figure 6.3.4.

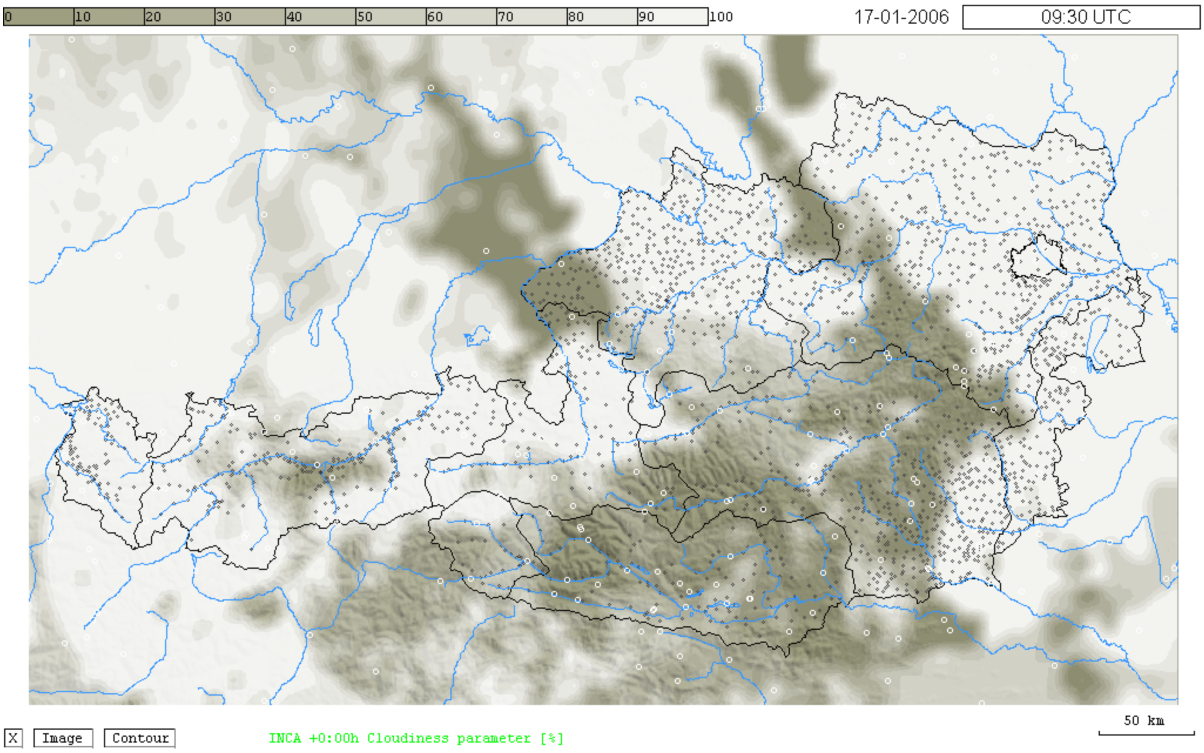

Figure 6.3.1: Operational SP analysis at 20060117, 0930Z.

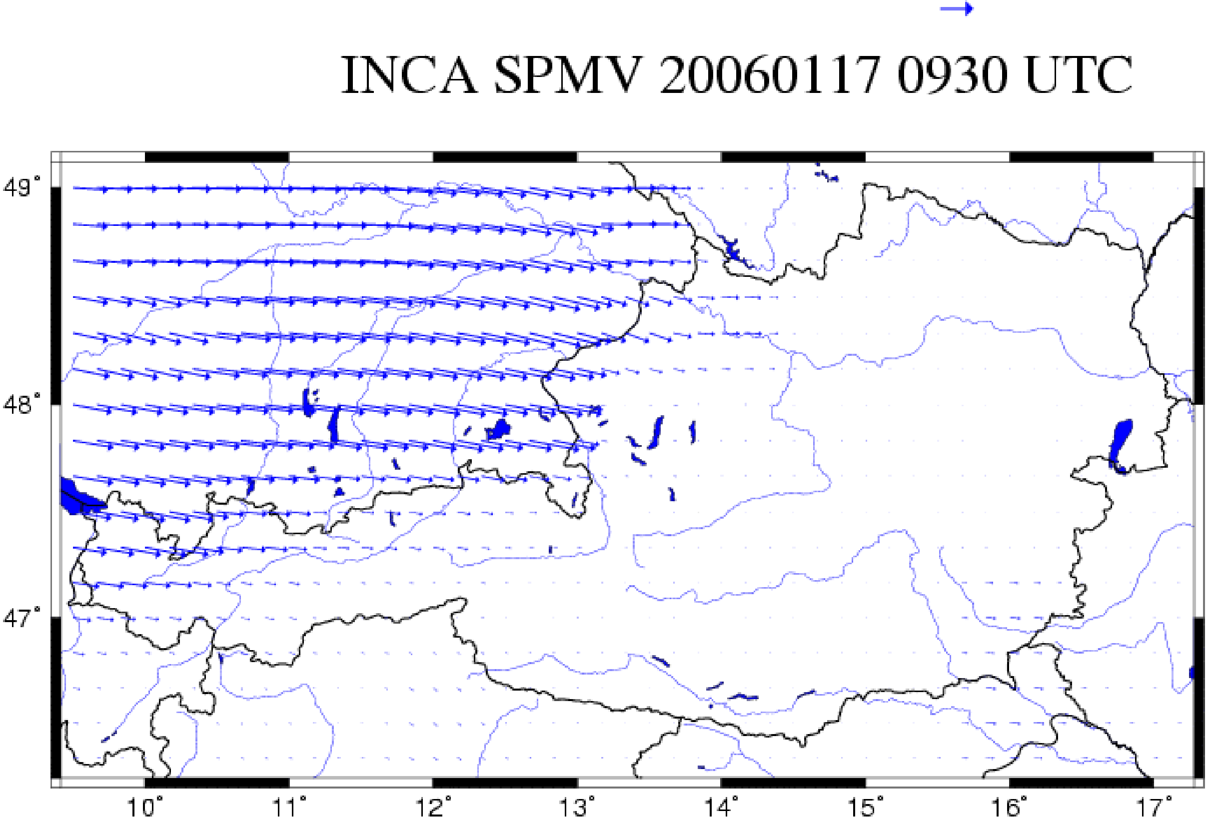

Figure 6.3.2: Mean motion vector field for extrapolation of SP analysis field at 20060117, 0930Z.

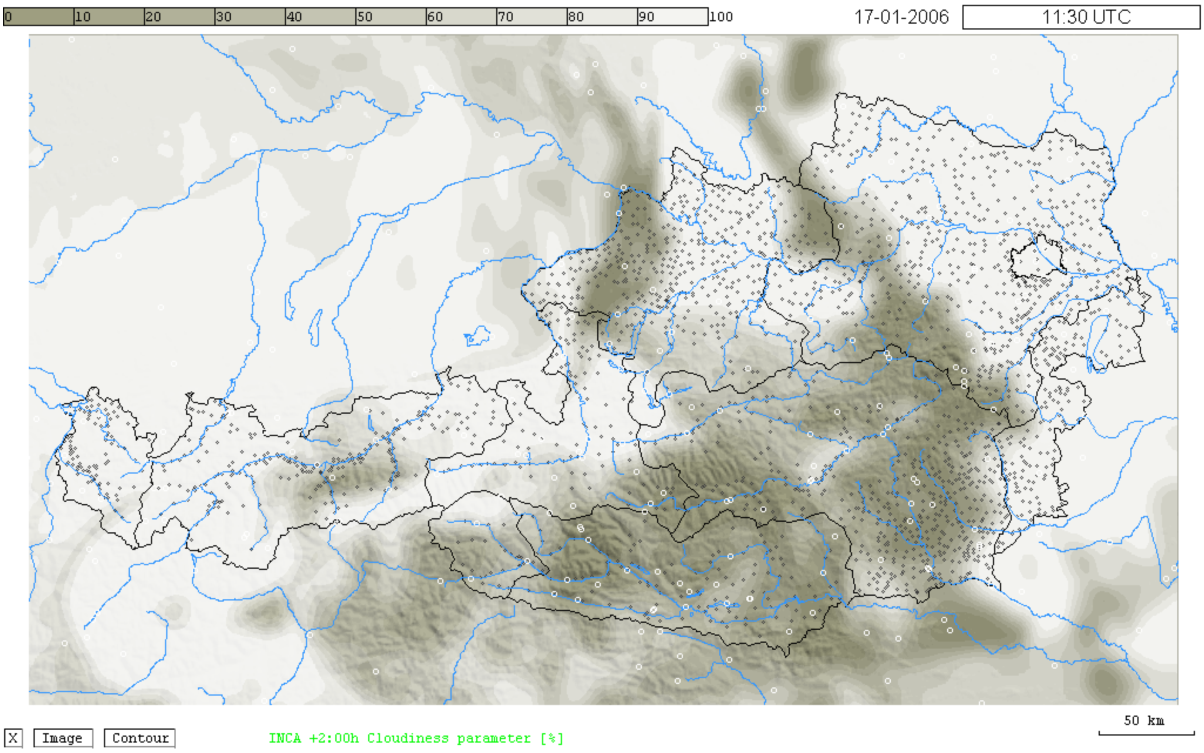

Figure 6.3.3: *SP* nowcasting field from 20060117 0930Z + 120min, extrapolated using the vector field shown in Figure 6.3.2.

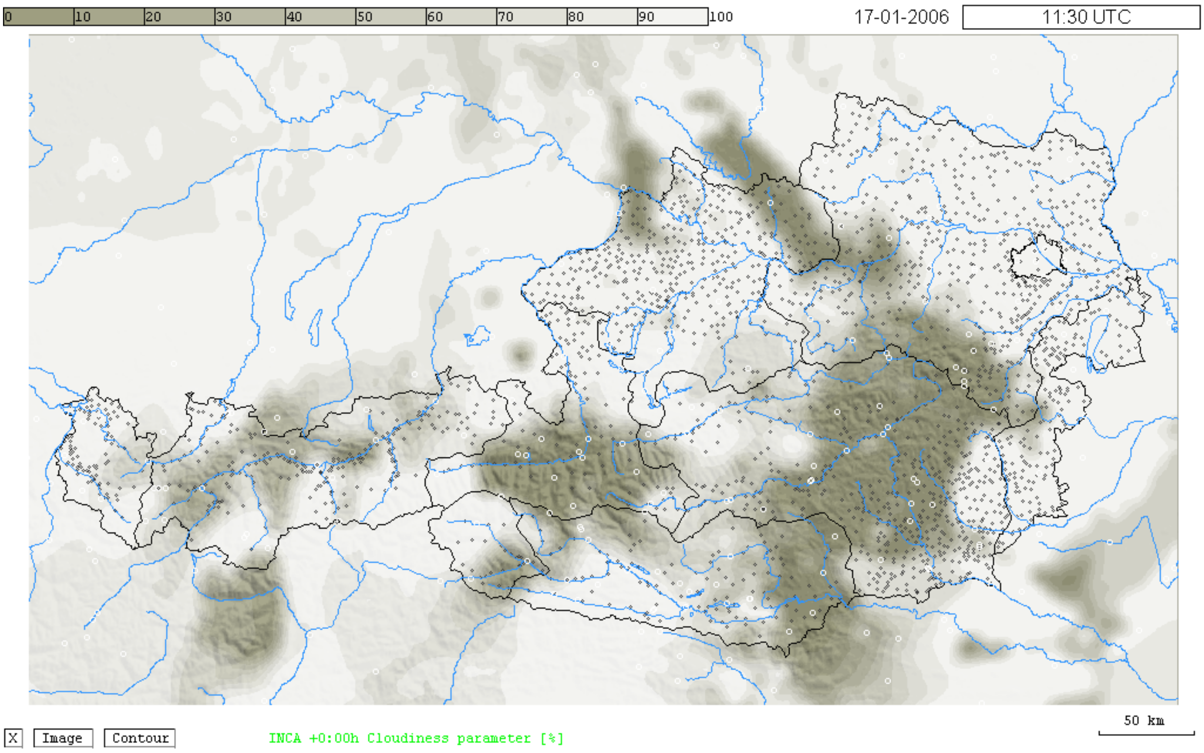

Figure 6.3.4: Verifying *SP* analysis field at 20060117 1130Z.

6.4 Precipitation

The INCA precipitation forecast consists of two components: (1) an observation-based extrapolation, and (2) an NWP model forecast. The extrapolation method is based on motion vectors determined from previous analyses. The model forecasts are output fields of the limited area model ALADIN and the global ECMWF model.

For observation-based extrapolation a number of different motion vectors were tested:

- Cloud motion vectors (CMVs),
- Radar motion vectors (RMVs),
- Water vapor motion vectors (WMVs),
- INCA motion vectors (IMVs),

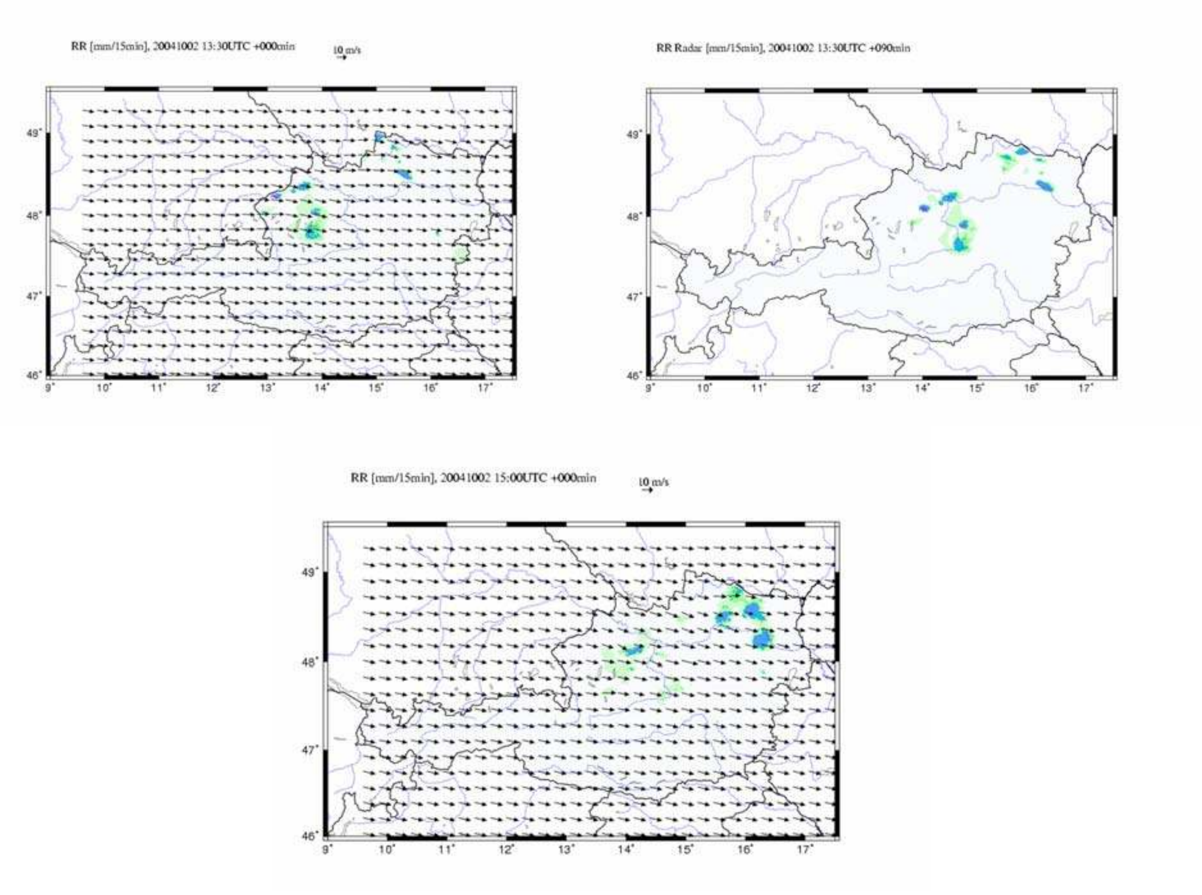

Figure 6.4.1: Example of a +1:30 h INCA precipitation nowcast using motion vectors. Upper left: analysis, upper right: nowcast, bottom: verifying analysis at +1:30 h.

The different sets of vectors have various advantages and disadvantages. The WMVs, for example, have the most complete areal coverage but indicate the motion at mid-tropospheric levels rather than at lower levels. RMVs are derived most directly from precipitation echo movement but are missing in many mountainous areas even if stations report precipitation there. The IMVs are derived from consecutive INCA precipitation analyses (Section 5d) and therefore provide the best consistency with the field they are applied to. Spurious correlations which would imply unrealistically large motion speeds are filtered meteorologically by comparison with ALADIN wind fields at 500 und 700 hPa. The filtering is done using the condition

$$\left|\vec{V}_{KORR}\right| + \left|\vec{V}_{KORR} - \vec{V}_{ALA}\right| \leq \left|\vec{V}_{ALA}\right| + 2\Delta\,, \qquad (6.4.1)$$

where $\vec{V}_{KORR}$ is the motion vector derived by correlation analysis, $\vec{V}_{ALA}$ is the ALADIN 500 or 700 hPa wind (whichever is closer to $\vec{V}_{KORR}$), and Δ is a prescribed wind speed scale which determines the amount of deviation permitted between $\vec{V}_{KORR}$ and $\vec{V}_{ALA}$. Operationally,

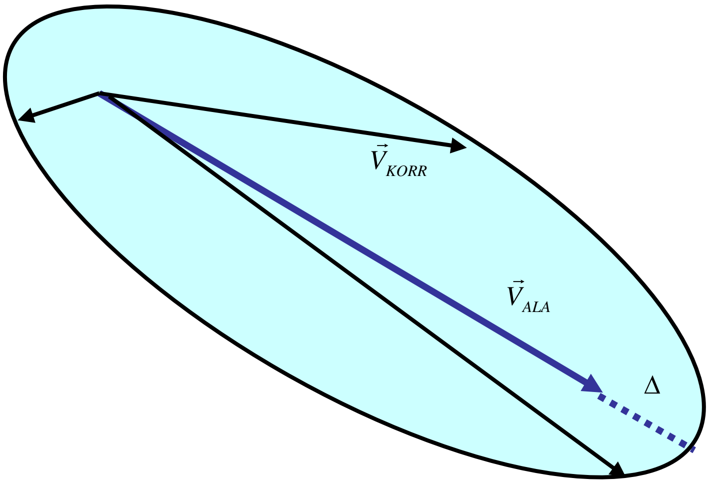

Figure 6.4.2: Meteorological filtering of motion vectors according to (6.4.1). The blue vector is the ALADIN 500 or 700 hPa wind. Black arrows show examples of motion vectors derived by the correlation algorithm. Motion vectors outside the elliptic area are rejected.

the value $\Delta = 5\,\text{ms}^{-1}$ is used. Eq. (6.4.1) defines an elliptic area as shown in Figure 6.4.2. It can be seen that precipitation patterns are allowed to move in the general direction of the model wind at any speed which is lower than the model wind (e.g. quasi-stationary upslope rain), at a speed which is somewhat larger than the model wind, and even slightly upstream. IMVs filtered according to (6.4.1) are used operationally to generate an extrapolation forecast of precipitation P_{EXTRAP}.

Verification of both point and areal forecasts of precipitation from INCA shows that on average extrapolation methods produce forecasts that are superior to NWP forecasts for ~2 hours. In order to obtain a continuous sequence of forecast fields a smooth transition from the extrapolation forecast P_{EXTRAP} to the NWP forecast is constructed through a prescribed weighting function. The currently operational weighting function gives full weight to the extrapolation forecast during the first 2 hours, decreases linearly to zero at 6 hours, and remains zero after that (Eqs.(6.4.3),(6.4.4)). In the future this prescribed weighting function will be replaced by a more general function based on error motion vectors (EMVs, cf. Section 7).

NWP models exhibit certain quasi-systematic errors in their precipitation forecasts, particularly in areas with pronounced topography. In the case of ALADIN and ECMWF the error characteristics are quite different which implies that the combination of both model outputs has some potential for reducing these errors. The issue has been investigated by using several years of archived areal precipitation forecasts and observations for 26 catchment-type areas in Austria and parts of Bavaria. In the study, emphasis was put on moderate and strong precipitation events (>5 mm /24 h and >10 mm /24 h in the areal mean, respectively). For each one of the 26 defined areas a linear relationship of the form

$$P_{OPT} = w_{ALA} P_{ALA} + w_{ECM} P_{ECM} \tag{6.4.2}$$

is determined, where the sum of the weights $w_{ALA} + w_{ECM}$ is not a priori constrained to equal 1. Optimal weights were found from the condition of minimal modified mean absolute error MAE*=MAE+0.5*|BIAS|. The optimal weights found for each area were spatially interpolated onto the INCA grid. The NWP model forecasts are also interpolated to this grid by bilinear interpolation. Thus a combined field P_{OPT} can be computed at each gridpoint operationally (Figure 6.4.3).

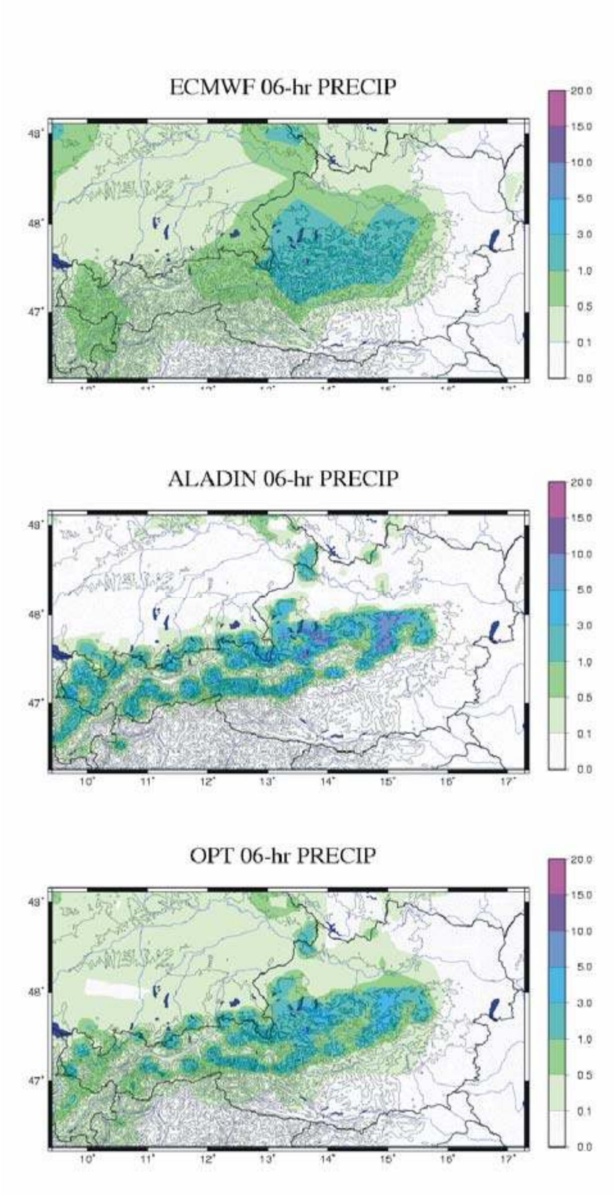
ECMWF 06-hr PRECIP

ALADIN 06-hr PRECIP

OPT 06-hr PRECIP

Figure 6.4.3: Example of an ‚OPT' precipitation forecast obtained from a spatially varying weighting of ALADIN and ECMWF forecasts. The OPT forecast gives improved amounts and more realistic spatial patterns than each model taken individually.

The INCA forecast of precipitation can be written in the form

$$P_{INCA}(t_i) = g\, P_{EXTRAP}(t_i) + (1-g)\, P_{OPT}(t_i)\,, \qquad (6.4.3)$$

where the weight function is given by

$$g(t_i) = \max\left(\min\left(1 - \frac{t_i - \tau_{p1}}{\tau_{p2} - \tau_{p1}}, 1\right), 0\right). \qquad (6.4.4)$$

Figure 6.4.4 shows a verification of areal precipitation forecasts over a 40-day period. On average, the forecast by the extrapolation method is better than the NWP forecasts during the first ~2 hours. This timescale generally varies between 1 and 6 hours, depending on the type of precipitation event, topographic characteristics etc.

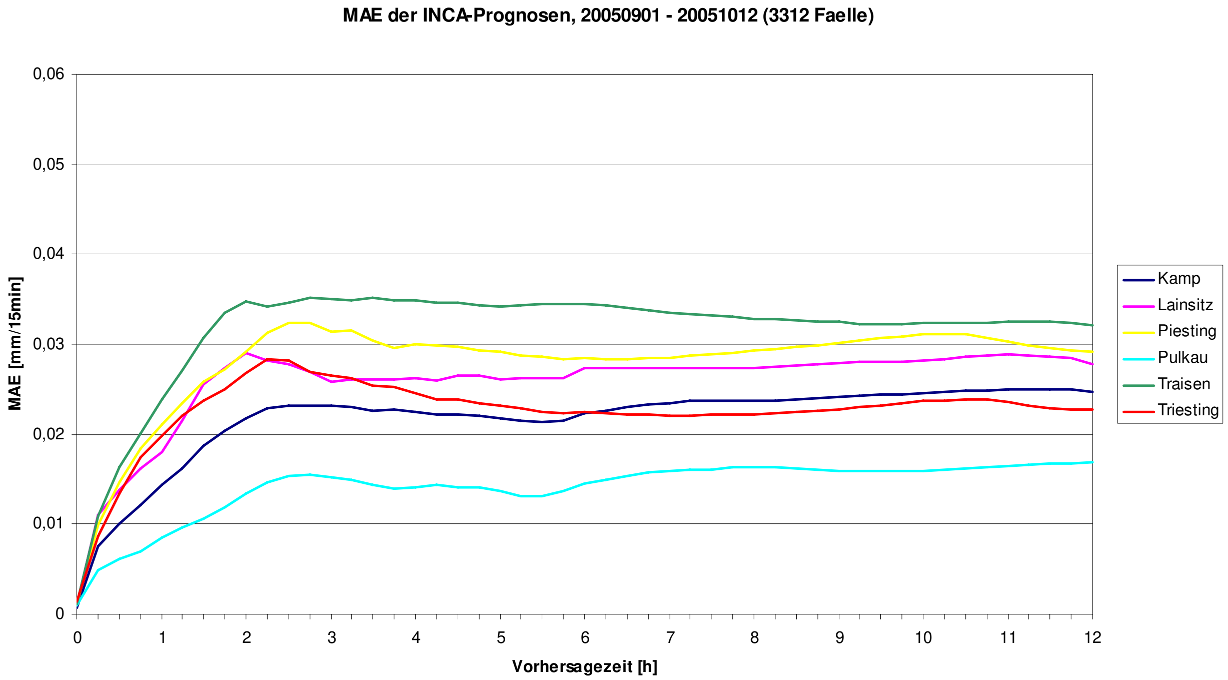

Figure 6.4.4: Mean absolute error of the INCA precipitation forecast (15-min amounts) as a function of lead time, for various small to medium-sized catchments in Lower Austria, over a 40-day period. The beneficial effect of the extrapolation forecast can be seen during the first ~2 hours.

6.5 Precipitation type

The method used to analyze snowfall line and precipitation type (see Section 5.5) is also applied to predicted temperature and humidity fields. Combined with predicted precipitation amounts, a nowcast of snowfall amounts is generated. Figure 6.5.1 shows an example of an INCA forecast of snowfall amount

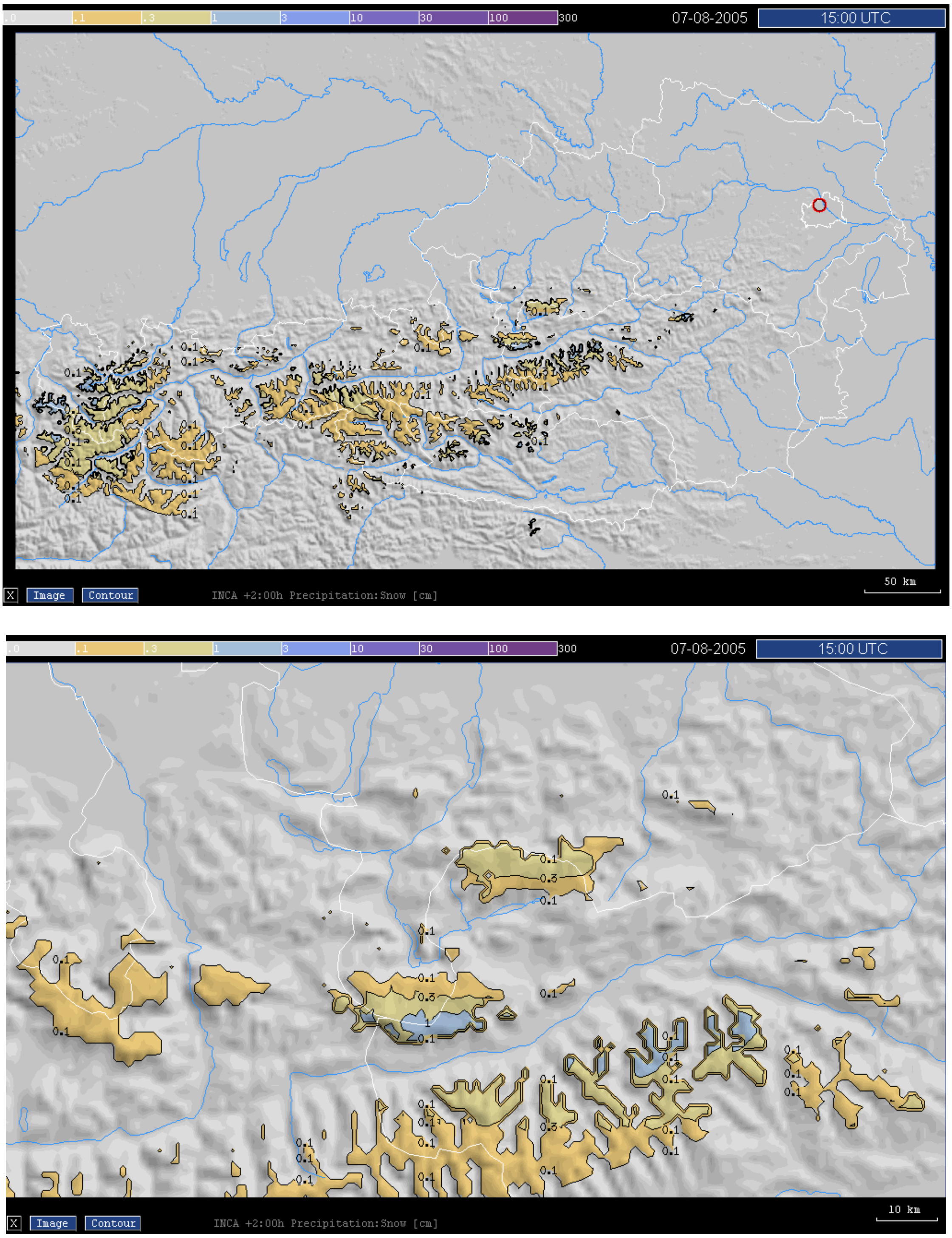

Figure 6.5.1: Example of an INCA nowcast of snowfall accumulation over the next 2 hours. Top: whole domain, bottom: zoom on Salzkammergut, near the centre of the domain.

7. INCA convective analysis fields

In order to improve the convective precipitation forecast beyond the currently used pure translational extrapolation, the evolution of convective cells (initiation, intensification, weakening, dissipation) must be assessed. In INCA, this evolution assessment will be based on convective analysis fields that are derived from the temperature, humidity, and wind analyses and nowcasts. The basic concept is to determine convective conditions in the area into which a convective cell is predicted to move, and give an estimate of the cell's intensity change based on these conditions. The diagnostic fields that are currently computed operationally are

- Lifted condensation level (LCL)
- Level of free convection (LFC)
- Convective available potential energy (CAPE)
- Convective Inhibition (CIN)
- Showalter index (SWI)
- Lifted index (LI)
- Trigger temperature (TTRIG)
- Trigger temperature deficit (DTTRIG=TTRIG-T)
- Equivalent potential temperature (THETA_E)
- Boundary layer flow convergence (CONV)
- Boundary layer humidity convergence (CONH)

(see examples in Figure 7.1). Initiation of new convective cells is related to fields like trigger temperature deficit and flow convergence. The evolution of existing cells depends on the presence of CAPE vs CIN in relation to the strength of the existing cell (as a measure of outflow strength). The ultimate goal is to design an algorithm which gives the probable evolution tendency of a cell or cluster of cells as a function of a subset of the fields above. This tendency would be superimposed on the pure translation already implemented in INCA. First results of a study along these lines can be found in Haiden and Steinheimer (2007).

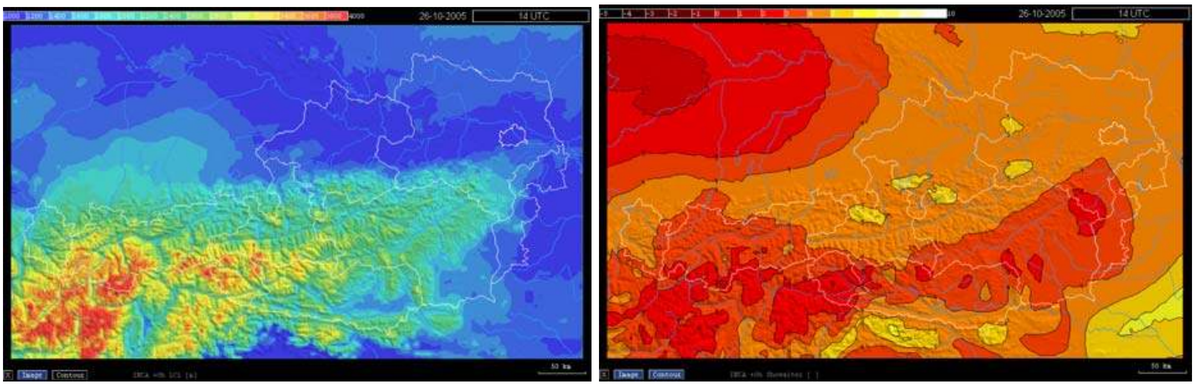

Figure 7.1: Example of INCA convective parameter analyses: LCL (left) and Showalter Index (right).

There exist several convective nowcast systems that can serve as a guideline for future developments in INCA. During the 2000 Sydney Olympics Forecast Demonstration Project (FDP) the following five systems were applied and evaluated:

1) TITAN (BMRC, Melbourne, Australien)
2) S-PROG (BMRC, Melbourne, Australien)
3) NIMROD (MetOffice, Exeter, Großbritannien)
4) GANDOLF (MetOffice, Exeter, Großbritannien)
5) ANC (NCAR, Boulder, CO, USA)

These systems use different methods of determining precipitation movement such as area tracking, individual cell tracking, and NWP model winds. Two of the systems (GANDOLF, ANC) have convective evolution and initiation capability (Wilson et al., 2004).

In the GANDOLF system, convective entities are classified into stages of development. Based on a conceptual model of storm evolution, future states are nowcast. New cells ('daughter' cells) can be initiated close to existing cells if the boundary layer convergence predicted by the NWP model is sufficiently strong. The ANC predicts cell initiation and evolution based on the interaction of existing storms and cumulus clouds with boundary layer convergence lines observed by radar, and NWP wind field characteristics. The major findings with regard to convective cell prediction in the Sydney FDP can be summarized as follows (Wilson et al., 2004). *1) Predictive skill above pure translation occurs when boundary layer convergence lines can be identified and used to nowcast cell evolution. 2) For nowcasts beyond 60 min, boundary characteristics are more important for storm initiation than early detection of cumulus clouds*.

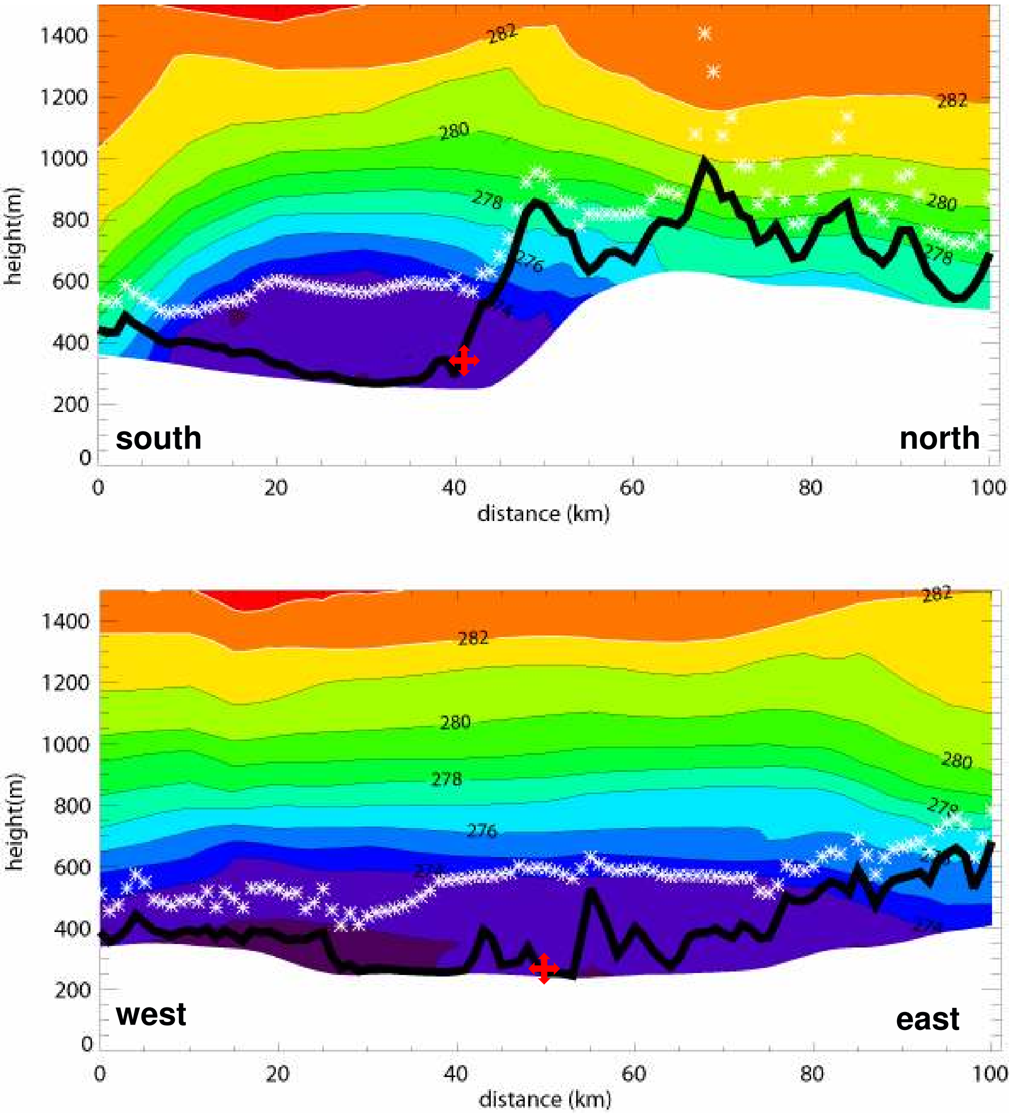

Figure 7.2: INCA potential temperature distribution within latitudinal and longitudinal vertical cross-sections across the Linz basin (Upper Austria) during a winter smog field campaign in February 2005. Black line shows INCA topography, white area indicates INCA valley floor surface. Mixing height is shown by white x's (Baumann-Stanzer, 2005).

For the development of a cell initiation and evolution module in INCA these results give a clear guideline and indicate the importance of a good wind field analysis. In Austria's alpine terrain, boundary layer convergence lines are to a large degree related to topography, which adds a deterministic component to cell initiation (Haiden, 2001a). With the current version of the INCA wind field analysis, the ability to correctly detect these convergence lines critically depends on the skill of the ALADIN model in predicting them, and on the surface station network to represent them. Case studies are carried out to determine to what extent this is in fact the case. However, none of the systems used for the Sydney FDP used convective analysis fields such as CAPE or CIN, so it remains to be investigated what additional benefit can be gained from their use.

Another application of INCA analysis fields with regard to convection is the assessment of boundary layer mixing heights for air pollution modelling. Figure 7.2 shows the INCA potential temperature distribution within latitudinal and longitudinal vertical cross-sections across the Linz basin (Upper Austria) during a winter smog field campaign in February 2005. Mixing heights were computed according to a Richardson number criterion.

8. Other derived fields

8.1 Icing potential

As part of Austria's contribution to COST727, an experimental numerical product for the analysis and forecast of icing potential is being developed. The icing potential indicates the rate of icing to be expected on structures due to contact freezing of supercooled cloud droplets. It is most likely at temperatures between 0°C and –20°C, and increases with cloud water content and wind speed. A first version of the computation of icing potential in INCA is based on the relationship

$$IP = 100 \cdot f_1(T) f_2(u) f_3(h), \tag{8.1}$$

where the functions for temperature T, wind speed u, and relative humidity h are given by

$$f_1(T) = \begin{cases} \exp\left[(T - T_{OPT2}) / T_{SCALE}\right] & T < T_{OPT2} \\ 1 & T_{OPT2} \le T < T_{OPT1} \\ T / T_{OPT1} & T_{OPT1} \le T < T_0 \\ 0 & T \ge T_0 \end{cases}, \tag{8.2}$$

$$f_2(u) = \min(1, u / u_{MAX}), \tag{8.3}$$

$$f_3(h) = \min\left[1, \max\left(0, \frac{h - h_{MIN}}{h_{MAX} - h_{MIN}}\right)\right]. \tag{8.4}$$

Since there is currently no analysis of liquid water content in INCA, relative humidity is used as a substitute to identify terrain which is likely inside a cloud, and temperature is used to qualitatively capture the decreasing amount of cloud liquid water in colder clouds. The rate of icing is assumed to increase linearly with wind speed up to a maximum wind speed above which the breaking off of ice is assumed to become a limiting factor. The parameters are currently set to the following values: T_0 = 0°C, T_{OPT1} = -3°C, T_{OPT2} = -20°C, T_{SCALE} = 10 K, u_{MAX} = 25 m/s, h_{MIN} = 95%, h_{MAX} = 100%. Figure 8.1 shows an example of icing potential as analyzed by INCA, as well as the three input fields.

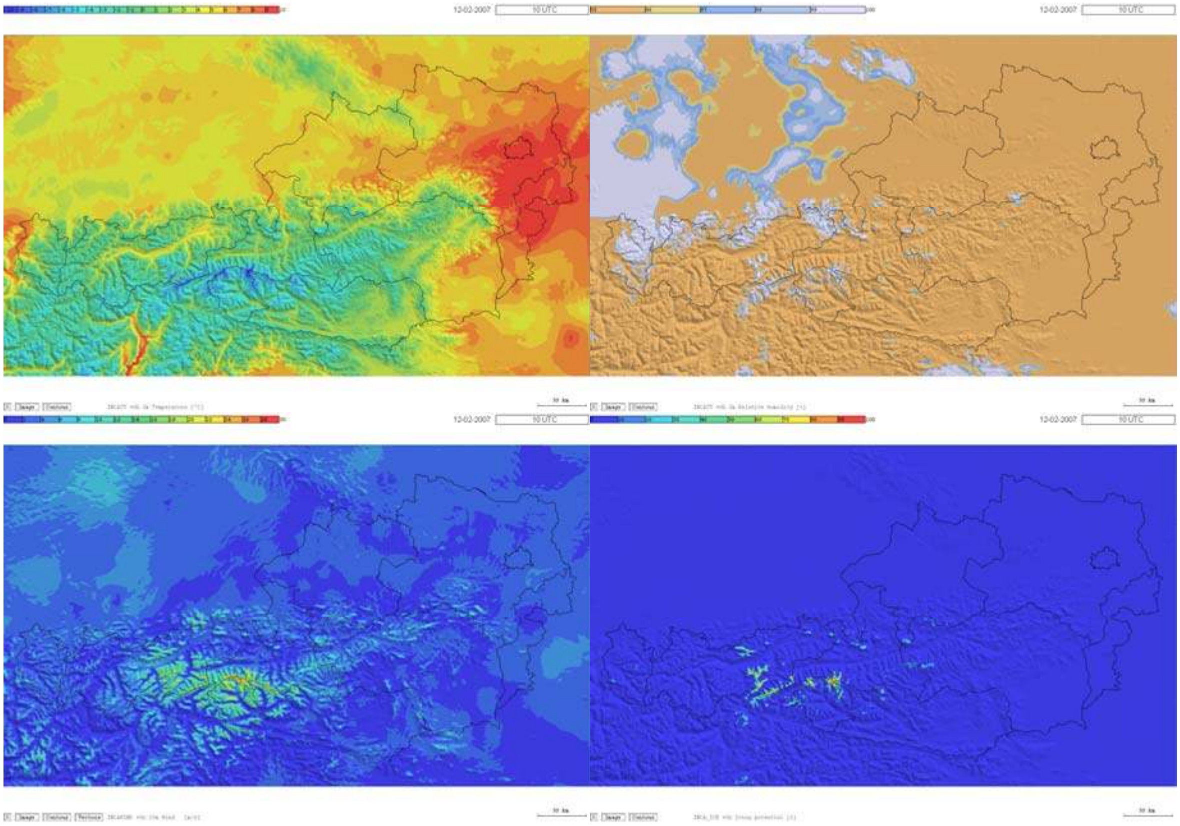

Figure 8.1: Example of an INCA analysis of icing potential (lower right). Also shown are the input fields: temperature (upper left), relative humidity (upper right), and wind speed (lower left). The icing potential indicates mountains where high wind speed combines with sufficient relative humidity at temperatures below zero.

8.2 Wind chill

In order to assess the physiological effect of a given combination of temperature and wind on the human body, especially at subzero temperatures, the wind chill is computed based on an updated relationship used by NOAA/NWS. In its original form it is given by

$$T_{wc}(T,V) = 35.74 + 0.6215T + V^{0.16}(0.4275T - 35.75)\,, \qquad (8.5)$$

where temperature T and wind chill T_{wc} are in degrees Fahrenheit, and wind speed V in mph. Converted to standard units, one obtains

$$T_{wc}(T,V) = 55.63 + 1.1187T + V^{0.16}(0.8753T - 25.10)\,, \qquad (8.5')$$

where temperature T and wind chill T_{wc} are in degrees Celsius, and wind speed V in m/s. Eq. (8.5) is an improved relationship compared to earlier versions and translates 10 m wind to the wind at human face level. It is based on a human face model and incorporates heat transfer theory. It does not take into account effects of the sun.

In INCA, (8.5') is applied at every gridpoint using 2 m temperature and 10 m wind. Since the formula can be applied only at wind speeds larger or equal 3 mph, we interpolate linearly between T and $T_{wc}(T,3)$ at smaller speeds, so that in the limiting case of zero wind the value T_{wc} = T is reproduced. Updated analyses and forecasts of wind chill are provided every hour.

8.3 Wind gusts

Based on the INCA mean wind analysis, a 24-h wind gust analysis has been implemented in order to provide daily maps of maximum wind speed during the latest 06Z-06Z period. The method employs the assumption of a gust factor that relates the mean wind speed to gust speeds and it uses gust speed observations from TAWES and SYNOP stations.

In a first step, the hourly INCA analyses of mean wind speed V_{ijn} are combined into a maximum mean wind speed analysis over the 24-h period by assigning to each gridpoint the maximum value found within the period. Here *i*, *j* are the grid indices in *x* and *y* direction, and *n* is the time index. A 1st-guess gust analysis G_{ij}^0 is created by multiplying this field with a constant gust factor (currently set to F_G =1.8).

$$G_{ij}^0 = F_G \max_n (V_{ijn}) . \tag{8.6}$$

Next, gust speeds are read from the observation database. These gust observations G_k^{OBS} are spatially interpolated, where in the horizontal, geometrical distance weighting is used, and in the vertical the distance weighting is performed in gust speed space. Thus, the weight of a gust observation for a given grid point becomes smaller the more the 1st-guess wind speed at that point differs from the 1st-guess wind speed at the station. The squared 'distance' between INCA gridpoint (*i,j*) and the *k*-th station is given by

$$r_{ijk}^2 = (x_k - x_i)^2 + (y_k - y_j)^2 + {c_G}^2 [G_{ij}^0 - G_k^0]^2 , \tag{8.7}$$

where the parameter c_G has the dimension of an inverse wind shear and is currently set to $2{\cdot}10^4$ s. This means that a distance of 1 m s^{-1} in gust space is equivalent to a horizontal distance of 20 km. In the actual implementation, the slightly modified version

$$r_{ijk}^2 = \max\left\{\Delta x \cdot \Delta y, (x_k - x_i)^2 + (y_k - y_j)^2 + {c_G}^2 [G_{ij}^0 - G_k^0]^2\right\} \tag{8.7'}$$

is used in order to avoid infinity in cases where a station by chance exactly coincides with a grid point. In INCA, the grid spacing is $\Delta x = \Delta y = 1$ km. The use of (8.7') also expresses the fact that differences of the distances between a grid point and two different stations which are smaller than 1 km are not considered significant. The resulting gust field is obtained from

$$G_{ij} = \frac{\sum_k \frac{G_k^{OBS}}{r_{ijk}^2}}{\sum_k \frac{1}{r_{ijk}^2}} \tag{8.8}$$

where the *k*-summation is extended over the 8 nearest stations. Note that 'nearest' in this context means smallest distance in the sense of (8.7').

As a precaution against possible underestimations of gust speed as a result of the nonlinear interpolation given by (8.7') and (8.8), the original 1st-guess gust field, scaled down using the minimum gust factor F_{GN} =1.2, is used as a lower threshold. Thus the final INCA gust analysis is given by

$$G_{ij}^{FINAL} = \max\left(G_{ij}, \frac{F_{GN}}{F_G} G_{ij}^0 \right) . \tag{8.9}$$

The parameter settings in the current INCA gust analysis have been chosen based on educated physical guesses and some case-study type experiments. They could (and should) be optimized. It should also be tested whether a height-dependent gust factor instead of a constant value increases the skill of the analysis. Generally, the skill of the analysis should be quantified using cross-validation.

8.4 Visibility

Another INCA analysis field which is still in the experimental stage, is visibility. It is assumed to vary linearly with the dewpoint deficit. Visibility (in m) is estimated using the heuristic relationship

$$VIS = \max\left[VIS_{MIN}, VIS_0 \left(SP + \frac{\Delta T_d^*}{\Delta T_{d0}} \right) \right], \tag{8.10}$$

where VIS_{MIN}=10 m is a the minimum visibility allowed, *SP* is the INCA insolation fraction (see Section 5.3), ΔT_{d0}=1.6 K is a dewpoint deficit scale, and ΔT_d^* is the modified dewpoint deficit given by

$$\Delta T_d^* = \begin{cases} 0 & \Delta T_d - \Delta T_{d\min} \le 0 \\ w \max\left[0, \Delta T_d - \Delta T_{d\min}\right] + (1-w)\Delta T_{d0} & \Delta T_d - \Delta T_{d\min} < \Delta T_{d0} \\ \Delta T_d - \Delta T_{d\min} & \Delta T_d - \Delta T_{d\min} \ge \Delta T_{d0} \end{cases} , \tag{8.11}$$

where $\Delta T_{d\min}$=0.4 K. It was found that dewpoint deficits below this value have no predictive power with regard to visibility. Eq. (8.11) takes into account the difference in behavior of the visibility/humidity relationship between low and higher elevations under conditions close to saturation. The weighting factor *w* depends on the height above valley floor according to

$$w = \frac{1}{\max\left\{1, \exp\left[(z - z_{val}) / H_{VIS1}\right]\right\}}, \tag{8.12}$$

where H_{VIS1}=500 m. At the height of the valley floor, *w*=1. At a height of 1500 m above valley floor $w \approx$0.05. Using (8.11)-(8.12), the transition from higher visibility values at drier conditions to minimum visibility at saturation is more abrupt at higher elevations. This is an attempt to account for the reduced aerosol content at higher elevations.

As can be seen from (8.10), the quantity VIS_0 is the visibility under overcast conditions (*SP*=0) when the dewpoint deficit is 2 K. It is not a constant but a function of absolute height given by

$$VIS_0 = VIS_{00} \max\left[1, \exp(z / H_{VIS2})\right], \tag{8.13}$$

where VIS_{00}=5000 m, and the visibility scaling height H_{VIS2}=2500 m. Thus, VIS_0 is close to 5 km at low elevations, and increases to ~17 km at an elevation of 3000 m. The current INCA visibility algorithm does not take into account the reduction of visibility due to precipitation. The various constants and scaling parameters have been chosen based on a limited set of observations. They have not yet been rigorously calibrated.

9. Summary and outlook

The first version of the INCA system became operational in 2005. In the years 2006-2008, several major extensions and modifications were made to the system, such as the additional field precipitation type, the use of a surface layer index in the temperature and humidity analysis, or the elevation dependence of precipitation. Based on station observations and remote sensing data it now provides three-dimensional hourly analyses and nowcasts of temperature, humidity, and wind, two-dimensional hourly analyses and nowcasts of global radiation, and two-dimensional 15-min analyses and nowcasts of precipitation, precipitation type, and cloudiness. It also provides hourly analyses of convective analysis fields such as LCL, CAPE, CIN, or moisture convergence. INCA fields are used operationally as input for flood forecasting systems in Austria, for various web portals used by customers of ZAMG (e.g. in the energy sector), and as a tool for the forecaster. The next steps of development will be

- Improved wind analysis, taking into account topographic anistropy.
- Improved wind nowcasting by moving from statistical extrapolation to dynamic trend extrapolation based on analysed pressure trends.
- Improved nowcasting of precipitation. The fixed weights for the merge of the nowcast with the ALADIN forecast should be replaced by adaptive weights responding to the most recent (last hours) forecast error of the ALADIN model.
- Implementation of an estimation of icing potential on structures (COST 727).
- Continuous automatic verification.
- Improved INCA portability by standardizing interfaces to observations.

Appendix A: Parameterization of the surface layer temperature surplus (deficit) scale [read_statdata()]

For the partitioning of the temperature observation correction into a surface layer part and a 'deep' contribution (Section 5.1), a temperature scale is computed which represents the maximum likely surface layer temperature surplus (deficit) under given meteorological conditions. The most important factors are insolation and wind speed. Ideally, a full surface layer parameterization based on boundary-layer physics should be used. However, this would be meaningful only if we also take into account local surface roughness and microtopographical characteristics at each station location in great detail. In order to avoid this complexity, we use a generalized, simplified approach which qualitatively takes into account the annual and diurnal variation of insolation and observed cloudiness and wind speed.

During daytime, DT_{SCALE} is parameterized as

$$DT_{SCALE} = \max\left(DT^{0}_{SCALE}, cH_{SFC} f_{SUN} f_{WIND}\right) \quad \text{(A.1)}$$

Where DT^{0}_{SCALE}=1 K, *c*=0.006 K/(W/m²), and the insolation and wind functions are given by

$$f_{SUN} = s/600, \quad \text{(A.2)}$$

$$f_{WIND} = \max\left[0, \exp\left(-\frac{V - V_0}{V_0}\right)\right]. \quad \text{(A.3)}$$

Here, *s* is the observed sunshine duration (seconds with direct insolation in the last 10 minutes), varying between 0 s with overcast, or at night, and 600 s under cloud-free daytime conditions. The parameter V_0=3 m/s. If the observed wind speed *V* exceeds this value, the wind function decreases, asymptotically going to zero for high wind speeds. Wind speeds smaller than V_0 are considered part of the convective circulations in the PBL on days with insolation and therefore not assumed to lead to a reduction of the surface layer temperature surplus.

The annual and diurnal variation of the surface sensible heat flux is parameterized as

$$H_{SFC} = H^{MIN}_{SFC} + (H^{MAX}_{SFC} - H^{MIN}_{SFC})\frac{1-\cos\left[\frac{\pi}{6}(m-0.7)\right]}{2}\max\left\{0, \cos\left[\frac{\pi}{l}(t-12)\right]\right\}, \quad \text{(A.4)}$$

where H^{MIN}_{SFC}=100 W/m², H^{MAX}_{SFC}=500 W/m², *l* is the seasonally varying length of the day in hours, *m* is the month, and *t* is the local time in hours.

The estimation of a physically plausible temperature deficit in the surface layer at night is much more difficult than the temperature surplus during the day. In suitable topographic settings (basin-type location) and with weak synoptic flow, inversions of 5 K and more can easily form within the lowest few dekameters. The maximum possible temperature deficit in a given night depends on atmospheric conditions, soil properties, and microtopographic characteristics such as the sky-view factor in a way that cannot be easily parameterized. Currently, the maximum surface layer temperature deficit at night is simply set to the constant value DT^{N}_{SCALE}=5 K.

Appendix B: Parameterization of lake effects on temperature [modify_T_over_lake()]

The parameterization of 2m temperature over lakes [LAKEMODE=1] is a weighted average of the hypothetical 2m temperature T_{hyp}^{INCA} without the presence of the lake, and the water surface temperature T^{LAKE}

$$T^{INCA} = wT^{LAKE} + (1-w)T_{hyp}^{INCA}\,, \tag{B.1}$$

where the weight *w*=0.3. If the water temperature is below 0 °C, ice cover is assumed. If at the same time the air temperature is below 0 °C as well, *w* is set to zero. In this case lake effects are assumed to vanish. Lake ice is not explicitly modeled, but taken into account by allowing the lake temperature to drop below zero. A lake temperature of -4 °C, for example, is equivalent to a certain amount of ice, and when the air temperature increases, a certain amount of energy is needed to get the lake temperature above 0 °C again (i.e. to melt the ice).

The time evolution of lake temperature is based on a simple force-restore model. The lake is regarded as a slow-responding heat reservoir, changes of which are forced by the difference between air and lake temperature

$$T^{LAKE}(t+\Delta t) = T_{\infty}^{LAKE} + [T^{LAKE}(t) - T_{\infty}^{LAKE}]\exp\left(-\frac{\Delta t}{\tau_{LAKE}}\right), \tag{B.2}$$

where the temperature towards which the lake temperature is asymptotically relaxed, is given by a weighted mean of air temperature and air dewpoint (each averaged over the area of the lake)

$$T_{\infty}^{LAKE} = a\overline{T^{INCA}} + (1-a)\overline{T_d^{INCA}}\,, \tag{B.3}$$

with *a*=0.85. If relative humidity is high, the asymptotic lake temperature is close to the air temperature. If relative humidity is low, the asymptotic lake temperature is lower than the air temperature. This crudely accounts for evaporative cooling of the lake surface. The timestep Δt = 1 h, the time-scale τ_{LAKE} is 12 h in the case of heating, and 72 h in the case of cooling. This accounts for the fact that if there is heating, the uppermost water layer is heated rather quickly, whereas cooling at the lake surface is communicated to greater depths by buoyancy-driven vertical overturning, leading to a larger response time.

The lake effect model is applied operationally to Lake Neusiedl in eastern Austria. It was found that despite its simplicity the prognostic lake temperature is usually quite close (typically to within 1 K) to the observed lake temperature. When available, the observed lake temperature is used to update the modeled lake temperature.

References

Baumann-Stanzer, K., 2005: Personal communication.

Browning, K. A., and C. G. Collier, 1989: Nowcasting of precipitation systems. *Rev. Geophys.,* **27,** 345-370.

Chamberlain, A. C., 1983 : Roughness length of sea, sand and snow. *Bound. Layer. Meteor.,* **25,** 405-409.

Cotton, W. R., and R. A. Anthes, 1989: *Storm and Cloud Dynamics*. Academic Press, San Diego, 880 pp.

Crook, N. A., and J. Sun, 2004: Analysis and forecasting of the low-level wind during the Sydney 2000 Forecast Demonstration Project. *Wea. Forecasting,* **19,** 151-167.

Daly, C., R. P. Neilson, and D. J. Phillips, 1994: A statistical-topographic model for mapping climatological precipitation over mountainous terrain. *J. Appl. Meteor.,* **33,** 140-158.

Frei, C., and C. Schär, 1998: A precipitation climatology of the Alps from high-resolution rain-gauge observations. *Int. J. Climatol.,* **18,** 873-900.

Golding, B. W., 1998: Nimrod: A system for generating automated very short range forecasts. *Meteorol. Appl.,* **5,** 1-16.

Haiden, T., 1995: Analytical solution of washout in stratiform clouds. *Contrib. Atmos. Phys.,* **68,** 3-14.

Haiden, T., 1997: An analytical study of cumulus onset. *Quart. J. Roy. Meteor. Soc*., **123,** 1945-1960.

Haiden, T., 1998: Analytical aspects of mixed-layer growth in complex terrain. Preprints*, Eighth Conference on Mountain Meteorology,* Amer. Meteor. Soc., Flagstaff, Arizona, 368-372.

Haiden, T., 2001a: High-resolution forecasts of mountain cumulus. Proceedings, *22nd EWGLAM / 7th SRNWP Meeting*, Toulouse, France, 134-138.

Haiden, T., 2003: On the pressure field in the slope wind layer. *J. Atmos. Sci*., **60,** 1632-1635.

Haiden, T., 2007: Predicting snowfall line and precipitation type from ALADIN forecasts. *ALADIN Newsletter,* **31**.

Haiden, T., and C. D. Whiteman, 2005: Katabatic flow mechanisms on a low-angle slope. J. Appl. *Meteor*., **44,** 113-126.

Haiden, T., and G. Pistotnik, 2008: Parameterization of elevation effects in short-duration precipitation analysis. Preprints, *13th Conference on Mountain Meteorology,* Amer. Meteor. Soc., Whistler, Canada, 4p.

Haiden, T., and G. Pistotnik, 2009: Intensity-dependent parameterization of elevation effects in precipitation analysis. *Adv. Geosci.,* **20,** 33-38.

Hand, W. H., 1996: An object-oriented technique for nowcasting heavy showers and thunderstorms. *Meteorol. Appl.,* **3,** 31-41.

Komma, J., C. Reszler, G. Blöschl, and T. Haiden, 2007: Ensemble prediction of floods - catchment non-linearity and forecast probabilities. *Nat. Haz. Earth Syst. Sci.,* **7,** 431-444.

Li, L., W. Schmid, and J. Joss, 1995: Nowcasting of motion and growth of precipitation with radar over a complex topography. *J. Appl. Meteor.,* **34,** 1286-1300.

Pierce, C. E., P. J. Hardaker, C. G. Collier, and C. M. Haggett, 2000: GANDOLF: a system for generating automated nowcasts of convective precipitation. *Meteorol. Appl.,* **7,** 341-360.

Pierce, C. E., E. Ebert, A. W. Seed, M. Sleigh, C. G. Collier, N. I. Fox, N. Donaldson, J. W. Wilson, R. Roberts, and C. K. Mueller, 2004: The nowcasting of precipitation during Sydney 2000: An appraisal of the QPF algorithms. *Wea. Forecasting,* **19,** 7-21.

Rauber, R. M., M. K. Ramamurthy, and A. Tokay, 1994: Synoptic and mesoscale structure of a severe freezing rain event: the St. Valentine's day ice storm. *Wea. Forecasting,* **9,** 183-208.

Seed, A. W., 2003: A dynamic and spatial scaling approach to advection forecasting. *J. Appl. Meteor.,* **42,** 381-388.

Sharples, J. J., M. F. Hutchinson, and D. R. Jellett, 2005: On the horizontal scale of elevation dependence of Australian monthly precipitation. *J. Appl. Meteor.,* **44,** 1850-1865.

Skoda, G., and N. Filipovic, 2007: Multi-data precipitation analysis. Austrian Academy of Sciences, Final report, Vienna, 17pp.

Smith, R. B., 1979: The influence of mountains on the atmosphere. *Advances in Geophysics,* Vol. 21, Academic Press, 87-230.

Steinacker, R., 1983: Diagnose und Prognose der Schneefallgrenze, *Wetter und Leben*, **35,** 81-90.

Steinacker, R., W. Pöttschacher, M. Dorninger, 1997: Enhanced Resolution Analysis of the Atmosphere over the Alps Using the Fingerprint Technique. *Annalen der Meteorologie*, **35,** 235- 237

Steinacker, R., M. Ratheiser, B. Bica, B. Chimani, M. Dorninger, W. Gepp, C. Lotteraner, S. Schneider, und S. Tschannett, 2006: Downscaling meteorological information over complex terrain with the fingerprint technique by using a priori knowledge. *Mon. Wea. Rev.,* **134,** 2758-2771.

Steinheimer, M., and T. Haiden, 2007: Improved nowcasting of precipitation based on convective analysis fields. *Adv. Geosci.*, **10,** 125-131.

Steppeler, J., H.-W. Bitzer, M. Minotte, and L. Bonaventura, 2002: Nonhydrostatic atmospheric modeling using a z-coordinate representation. *Mon. Wea. Rev.,* **130,** 2143-2149.

Stull, R. B., 1988: *An Introduction to Boundary Layer Meteorology*. Kluwer, 670pp.

Sun, J., and N. A. Crook, 2001: Real-time low-level wind and temperature analysis using WSR-88D data. *Wea. Forecasting,* **16,** 117-132.

Wang, Y., T. Haiden, and A. Kann, 2006: The operational limited area modelling system at ZAMG: ALADIN-AUSTRIA, *Österr. Beiträge zu Meteorologie und Geophysik*, Heft 37, 33p.

Whiteman, C. D., T. Haiden, B. Pospichal, S. Eisenbach, and R. Steinacker, 2004: Minimum temperatures, diurnal temperature ranges and temperature inversions in limestone sinkholes of different sizes and shapes. *J. Appl. Meteor.*, **43,** 1224-1236.

Wilson, J. W., and W. E. Schreiber, 1986: Initiation of convective storms by radar-observed boundary layer convergence lines. *Mon. Wea. Rev.,* **114,** 2516-2536.

Wilson, J. W., E. E. Ebert, T. R. Saxen, R. D. Roberts, C. K. Mueller, M. Sleigh, C. E. Pierce, and A. Seed, 2004: Sydney 2000 Forecast Demonstration Project: Convective storm nowcasting. *Wea. Forecasting,* **19,** 131-150.